Department MATHEMATIK

FRIEDRICH-ALEXANDER UNIVERSITÄT ERLANGEN-NÜRNBERG
NATURWISSENSCHAFTLICHE FAKULTÄT

PREPRINT-REIHE
ANGEWANDTE MATHEMATIK
des Departments Mathematik

Friedrich-Alexander-Universität Erlangen-Nürnberg

Numerical investigation of a fully coupled micro-macro model for mineral dissolution and precipitation

von

N. Ray, J. Oberlander & P. Frolkovič

No. 400 2018

Department Mathematik
– Bereich Modellierung, Simulation, Optimierung –
Cauerstraße 11
91058 Erlangen

Geschäftsstelle:

Tel.: +49 9131 85-67063
Fax: +49 9131 85-67065

Internet: `http://www.am.uni-erlangen.de`

ISSN 2194-5127, 18.12.2018, No. 400

Numerical investigation of a fully coupled micro-macro model for mineral dissolution and precipitation

Nadja Ray* Jens Oberlander* Peter Frolkovič†

December 18, 2018

Abstract

Mineral dissolution and precipitation alter a porous medium's structure and its bulk properties. Due to the medium's heterogeneity and lacks in dynamic pore-scale measurements, there has been an increasing interest in comprehensive models accessing such phenomena on the macroscale without disregarding available pore-scale information. Such micro-macro models may be derived from detailed pore-scale models applying upscaling techniques and comprise several levels of couplings. Our model consists of transport equations at the scale of the porous medium (macro scale) while taking the processes of convection and diffusion into account. They include averaged time- and space-dependent coefficient functions which are in turn explicitly computed by means of auxiliary cell problems (micro scale). Structural changes due to dissolution and precipitation reactions result in a time- and space dependent domain on which cell problems are defined. The interface between the mineral and the fluid and consequently the explicit geometric structure is characterized by means of a level-set. Here, information from the transport equations solutions is taken into account (micro-macro scale). A numerical scheme is introduced which enables evaluating such complex settings. For the level set equation an upwind scheme by Rouy and Tourin is applied. An eXtended Finite Element Method is used for the evaluation of the cell problems while the transport equations are solved applying Mixed Finite Elements. Ultimately, we investigate the potentially degenerating bulk properties of the medium such as porosity and effective diffusion. Moreover, we apply our approach to the dissolution of an array of calcite grains in the micro-macro context and validate our numerical scheme.

1 Introduction

Porous media applications naturally exibit different spatial scales, on which measurements, modeling and simulations are possible. At least two scales are commonly identified with a porous medium: the micro/pore-scale and the macro/continuum scale. The pore scale is the fundamental scale where processes take place with pore (void) space and solid being distinguishable. On the other hand, the continuum scale, i.e. the scale of the porous medium, is ultimately of practical relevance for reliable reactive transport computations. However, geochemical behavior cannot be understood considering this larger scale alone and investigations become increasingly difficult if the dynamically evolving pore scale structure is taken into account. In [45], a review of the current state of pore-scale geochemical processes, latest experimental techniques for the microscopic characterization and quantification of porous medium structure and texture as well as reactive transport modeling on different scales is found.

Modeling approaches include pore-scale models [4, 21, 54], pore network models [52], hybrid models [30, 2, 47], micro-continuum models [44, 42, 43], micro-macro models resulting from averaging theory [1, 24], and purely continuum models; for further references see also [45]. Each approach has its advantages and disadvantages: Pore scale models directly take into account the spatial heterogeneity obtainable for instance from advanced imaging techniques. Although imaging techniques have made tremendous progress and

*Chair of Applied Mathematics I, Department of Mathematics, Friedrich-Alexander Universität Erlangen-Nürnberg, Cauerstr. 11, 91058 Erlangen, Germany, Tel.: +49-9131-67211, ray@math.fau.de

†Dept. of Mathematics and Descriptive Geometry, Faculty of Civil Engineering, Slovak University of Technology, Radlinskeho 11, 81005 Bratislava, Slovakia, Tel.: +421 259274 719, peter.frolkovic@stuba.sk

pore-scale structures and textures may be captured quite well, dynamic imaging is still a challenge. Moreover, accurate simulation results are obtainable only for small spatial and temporal resolutions even with high-performance computing. What is more, only pixelized, i.e. unphysical representations of interfaces are given by (micro) CT-images, cf. [13] for an energy-based solution strategy in the phase field context. Pore network models are mesoscale models which are valid up to the scale, on which continuum models are applicable. However, the simplicity and quality of the chosen representative structures may be a source of inaccuracy and have a large impact on the predictive value. Hybrid models may combine different types of models such as discrete and continuum models and/or separate the computational domain in pore-scale and continuum scale subdomains, which are bidirectionally coupled via boundary conditions or small overlapping handshake domains. The latter models are not reasonable for all kinds of applications, particularly if processes leading to the alteration of the structure are not locally restricted. Likewise, in dual porosity models, equations that are valid on different scales are combined. Flow is for instance described by a combination of Stokes equations (for the void) and Darcy equation (for the porous matrix) which together are then termed Brinkman equation, cf. [44, 42, 43] for recent applications including mineral dissolution. Such microcontinuum models are a useful tool where computational expensive pore-scale models are not feasible. However, they have the drawback of not resolving interfaces accurately. Furthermore, they always need a parametrization in terms of the medium's bulk properties which is also true for purely continuum models. Consequently, combinations with heuristics or stand alone pore-scale modeling are most often used. This approach, however, disregards the intimate link between the two tightly coupled scales.

In contrast to this perception, we focus on bidirectionally coupled micro-macro models explicitly capable of evolving interfaces. Classically, interfaces may be described by phase field methods and level set methods, cf. [21] in the context of pore-scale dissolution/precipitation reactions. Phase field models are widely used since they are analytically more accessible than level set methods which on the other hand directly yield a description of the evolving sharp interface. In the context of micro-macro models, a dynamic bidirectional communication between the evolving micro/pore scale and the macro/continuum scale may be derived through upscaling techniques. The upscaling of phase field models was performed to investigate dendritic growth [8], three phase systems in the absence of flow [33] and two-phase/unsaturated flow [37, 36, 5]. On the other hand, an extension of formal, two-scale, asymptotic expansion including a level set description for an evolving solid-fluid interface was introduced in [49, 24]. This method has been applied to precipitation/dissolution reactions [49, 24, 25], locally periodic media [23], biofilm growth [7, 38, 39], colloid dynamics [28], drug delivery [29], and reactive flows under dominant convection in [18, 31].

In this research, we numerically investigate a micro-macro model similar to that stated in [24], which was derived from a detailed pore-scale model applying upscaling via two-scale asymptotic expansion in a level-set framework [24]. In this model, mineral precipitation and dissolution reactions alter the porous mediums' structure. More precisely dissolved chemical species c_i are transported by convection and diffusion through the porous medium and react to a mineral with non-negligible volume fraction and density ρ. At the pore-scale, such reactive transport models have been considered by [53] in the case of (nearly) circular dissolution, where phase-field and level set approaches were compared. Likewise, [50] compared level set and pore network models for small pore networks and showed the pore network models' applicability to geometries extracted from real microtomography data. [51] investigated reactive transport with first-order kinetics in a level set framework for simple media such as parallel planes and arrays of cylinders and also for realistic random porous media. Further investigations by means of level-set methods was undertaken in [19, 20] with a focus on precipitation in a pore throat and a fractured porous medium. Finally, [22] investigated the dissolution of (an array of) calcite grains and the preferential dissolution of mineral composites, again by means of level set methods at the pore-scale and sophisticated reaction rates according to the transition state theory.

To access larger scales as well, we focus on micro-macro models instead of pore scale models. The micro-macro model consists of transport equations for the species' concentrations at the scale of the porous medium (macro scale), taking the processes of convection and diffusion into account. The transport equations include the

averaged time- and space-dependent parameters of porosity, specific surface, and effective diffusion tensor, which is in turn explicitly computed by means of auxiliary cell problems (micro scale). Structural changes due to the dissolution and precipitation reactions result in a time- and space dependent domain, on which cell problems are defined. The interface between the mineral and the fluid and consequently the explicit geometric structure is characterized by means of a level set. Here, information from the transport equations solutions is taken into account (micro-macro scale). Since the overall model comprise several levels of couplings, cf. Figure 2, thus far only very restrictive geometrical settings, e.g. radially symmetric situations, have been investigated numerically [24, 40]. This has led to a greatly simplified set of equations: Instead of the level-set equation, an ordinary differential equation is solved and coupled to the partial differential equations for transport.

In this paper, we novelly address the numerical investigation of the full problem including the level-set equation. As a proof of concept, we study a simple micro-macro problem based on the clogging of a single pore (motivated by [19]) as well as on the dissolution of an irregularly structured mineral composite (cf. [9]). In these situations, topological changes in the pore scale structure arise, which result in terminating/initializing the degeneration of bulk transport properties. We further illustrate this impact on macroscale transport. Ultimately, we investigate the dissolution of an array of calcite grains as described in [22], but this time in the micro-macro context. The evolution and the strong coupling of scales generally necessitates solving as many cell problems as there are elements in the discretization on the macro scale. However, in the situation of a small Peclet or Damkohler number, a drastic reduction in complexity is possible since it then becomes evident that compact or uniform dissolution takes place; see [17] for a thorough investigation of dissolution regimes with a focus on wormhole formation and [1, 2] for a study on the validity of upscaled models in different regimes.

To reduce the computational effort arising from the introduction of multiple cell problems, we split the macroscopic domain into a problem-dependent partition of subdomains (vertical slices), cf. Figure 14. For each subdomain, we consider only one, but evolving microscopic unit cell. We study the impact of the number of subdomains on the approximation quality. As discretization methods, we apply an upwind scheme by Rouy and Tourin [34] to the level-set equation. EXtended Finite Element Methods are used to evaluate the cell problems and Mixed Finite Elements are applied for solving the transport equation. We quantitatively validate our numerical scheme and address the applicability of Newton's method. If applicable an ansatz similar to the one proposed in [15] is applied to include the impact of the magnitude and direction of the flow velocity on the dissolution pattern.

Outline: In Section 2, a pore-scale model including dissolution/precipitation reactions, the method of formal two-scale asymptotic expansion in a level-set framework, and the micro-macro model obtained are stated. In Section 3, the discretization methods are discussed. In Section 4, various illustrative examples are investigated numerically to show the feasibility of our approach: First, the clogging of a single pore is investigated (Section 4.1) and second, the dissolution of a mineral composite is considered (Section 4.2). For both scenarios, the impact on bulk transport properties and macroscopic transport is visualized in Section 4.3. Thereafter in Section 4.4, the dissolution of an array of calcite grains as an example of a fully coupled micro-macro problem is investigated with the outcome being discussed quantitatively.

2 Mathematical model

2.1 Geometrical setting

As underlying geometry, we consider a bounded and connected domain $\Omega \subset \mathbb{R}^2$ with exterior boundary $\partial\Omega$ and an associated periodic microstructure. The microstructure is defined by unit cells $Y = \left[-\frac{1}{2}, +\frac{1}{2}\right]^2$ being composed of a solid part Y_s and a fluid part $Y_l := Y \backslash \bar{Y}_s$ with solid-fluid interface $\Gamma = \bar{Y}_l \cap \bar{Y}_s$. We define the scaling parameter $\varepsilon \ll 1$ and assume that the macroscopic domain Ω initially is an ideal porous medium and is therefore decomposed in scaled unit cells $Y_\varepsilon = \varepsilon Y$ that are shifted in such a way that their midpoints (i, j) coincide with a regular mesh of size ε. The scaled and shifted cells, which are denoted by Y_ε^{ij}, are divided into an analogously scaled fluid part $Y_{\varepsilon,l}^{ij}$ and solid part $Y_{\varepsilon,s}^{ij}$. The scaled and shifted solid-fluid interface is denoted by Γ_ε^{ij} with the unit outer normal ν_ε. The time-dependent initially connected fluid part/pore space, the solid part, and the interior boundary of

the porous medium are defined by

$$\Omega_\varepsilon := \bigcup_{i,j} Y^{ij}_{\varepsilon,l}, \quad \Omega\backslash\overline{\Omega}_\varepsilon := \bigcup_{i,j} Y^{ij}_{\varepsilon,s},$$
$$\text{and} \quad \Gamma_\varepsilon := \bigcup_{i,j} \Gamma^{ij}_\varepsilon.$$

2.2 Pore-scale model

A level set is capable characterizing the fluid phase/pore space of a saturated porous medium via

$$L(t,x) = \begin{cases} < 0 & \text{fluid phase/pore space,} \\ = 0 & \text{interface,} \\ > 0 & \text{solid phase.} \end{cases}$$

In the context of periodic porous media as introduced in Section 2.1, the level-set L_ε fulfills the following ε-scaled partial differential equation, [26]

$$\begin{aligned} \partial_t L_\varepsilon + v_{n,\varepsilon}|\nabla L_\varepsilon| = 0 \qquad & x \in \Omega,\ t \in (0,T), \\ L_\varepsilon(0,.) = L^0 \qquad & x \in \Omega \end{aligned}$$

with the normal velocity of the interface $v_{n,\varepsilon}$ and initial value L^0. In order to close the model, constitutive assumptions for the velocity $v_{n,\varepsilon}$ must be made. For dissolution and precipitation reactions, it is reasonable to relate the velocity $v_{n,\varepsilon}$ to the reaction rate f, cf. Section 4.4.

In case of heterogeneous reactions with rate f, the scaled transport equation for the species' concentration c_ε reads [24]

$$\begin{aligned} \partial_t c_\varepsilon - \nabla\cdot(-v_\varepsilon c_\varepsilon + D\nabla c_\varepsilon) = 0, & \\ x \in \Omega_\varepsilon(t),\ t \in (0,T), & \\ (-v_\varepsilon c_\varepsilon + D\nabla c_\varepsilon)\cdot\nu_\varepsilon - \varepsilon\alpha f(c_\varepsilon,\rho)(c_\varepsilon-\rho) = 0, & \\ x \in \Gamma_\varepsilon(t),\ t \in (0,T), & \\ (-v_\varepsilon c_\varepsilon + D\nabla c_\varepsilon)\cdot\nu = 0, & \\ x \in \partial\Omega,\ t \in (0,T), & \\ c_\varepsilon = c^0, & \\ x \in \Omega_\varepsilon(0) & \end{aligned}$$

with molecular diffusion D, mineral density ρ, and $\alpha = 1/\rho$. The mass conservation law is applied on the interior interface under the assumption that the interface cannot hold mass and a no-flux boundary condition is applied on the exterior boundary. The velocity v_ε in the advective term may either be prescribed, or be determined e.g. from the incompressible Stokes equations with no-slip boundary conditions on the evolving interface, see [24]. Finally, the initial conditions c^0 for the concentration supplements the model.

2.3 Upscaling

To formally identify the limit $\varepsilon \to 0$, the method of two-scale asymptotic expansion is applied. A mathematical description can be found, e.g., in [3] and [35]. Concerning the scale separation, besides the global variable x, a microscopic variable y is introduced. Both are connected via the relation $y = x/\varepsilon$. As a consequence, the expansion of the spatial gradient reads

$$\nabla_\varepsilon = \nabla_x + \frac{1}{\varepsilon}\nabla_y.$$

Furthermore, it is assumed that all variable functions can be expanded in series of the scale parameter ε, i.e.

$$\begin{aligned} \varphi_\varepsilon(t,x) = \varphi_0(t,x,y) + \varepsilon\varphi_1(t,x,y) & \\ + \varepsilon^2\varphi_2(t,x,y) + \dots, & \\ y = x/\varepsilon, \quad \varphi_\varepsilon \in \{v_\varepsilon, c_\varepsilon\}. & \end{aligned}$$

Additionally to the standard expansions introduced above in the framework of a level set description also the level set L_ε itself and the normal vector ν_ε have to be expanded due to the evolving microstructure. For a two-dimensional setting the expansion of the normal vector can be expressed in terms of the level set and the following expressions are obtained, see [24]:

$$\begin{aligned} L_\varepsilon(t,x) = L_0(t,x,y) + \varepsilon L_1(t,x,y) & \\ + \varepsilon^2 L_2(t,x,y) + \dots, & \\ y = x/\varepsilon, & \end{aligned}$$

$$\nu_\varepsilon = \nu_0 + \varepsilon\nu_1 + O(\varepsilon^2),$$
$$\nu_0 = \frac{\nabla_y L_0}{|\nabla_y L_0|}, \qquad \nu_1 = \tau_0 \frac{\tau_0\cdot(\nabla_x L_0 + \nabla_y L_1)}{|\nabla_y L_0|}$$

with $\tau_0 := \nu_0^\perp$. Applying these expansions to our problem and analyzing the different orders in ε^k, $k \in \mathbb{Z}$ the desired macroscopic homogenized problem description is obtained, cf. [24]:

Theorem 1. *The leading order expansion of the level set describes the leading order time evolving domain* $Y_{l,0}(t,x) := \{y : L_0(t,x,y) < 0\}$ *and interface* $\Gamma_0(t,x) := \{y : L_0(t,x,y) = 0\}$ *at the microscale. The leading order concentration* c_0 *and*

level set L_0 fulfill the following micro-macro limit problem:
The transport equation for the concentration c_0 reads

$$\begin{aligned}\partial_t(\phi c_0) + \nabla_x \cdot (\overline{v}_0 c_0) - \nabla_x \cdot (\mathbb{D}\nabla_x c_0) \\ = -\sigma f(c_0, \rho) \text{ in } \Omega\end{aligned}$$

with porosity $\phi = \frac{|Y_{l,0}|}{|Y|}$, specific surface $\sigma = \frac{|\Gamma_0|}{|Y|}$, and diffusion tensor $\mathbb{D}$ defined as

$$\mathbb{D}_{ij} := \int_{Y_{l,0}(t,x)} D\left(\partial_{y_i}\zeta_j + \delta_{ij}\right) dy \tag{3}$$

and ζ_j being the solutions to the supplementary family of cell problems for $j = 1, 2$

$$\begin{aligned}-\nabla_y \cdot (\nabla_y \zeta_j) &= 0 && \text{in } Y_{l,0}(t,x), \\ \nabla_y \zeta_j \cdot \nu_0 &= -e_j \cdot \nu_0 && \text{on } \Gamma_0(t,x), \\ \zeta_j &\text{ periodic in } y, \\ \frac{1}{|Y|}\int_{Y_{l,0}} \zeta_j \, dy &= 0.\end{aligned}$$

Furthermore, the level set fulfills

$$\partial_t L_0 + v_{n,0}|\nabla_y L_0| = 0 \qquad \text{in } Y \times \Omega.$$

In the upscaled model, a prescribed velocity or Darcy's velocity $\overline{v}_0$ as derived in [24] may be used. We further emphasize that the macroscopic variable x enters the microscale problems as a parameter which leads to a bidirectional coupling of the micro-macro problem as illustrated in Figure 2.

3 Numerics

The fully coupled micro-macro problem as introduced in Theorem 1 in Section 2 must now be solved efficiently. The evolution and the strong coupling of scales makes it in general necessary to solve as many cell problems as there are elements in the macroscale discretization in each time step in order to evaluate the macroscopic parameters accurately. This quickly leads to a large number of cell problems which significantly increases the runtime of any simulation. Thus, the numerical discretization must be chosen such that the compromise between accuracy and runtime overhead is sufficiently met. Different approaches are available to reduce the computational burden. Besides parallelization of the code in order to solve the cell problems simultaneously, offline precomputations as performed in [13], adaptive strategies as discussed in [32] in the phase field context, or the integration of physical information leading for instance to uniformity in one spatial direction may be applied. The situation in Section 4 enables us applying the latter approach to the micro-macro problem.

We now introduce the discretization methods used for each subproblem and outline the overall algorithm to capture the complexity of the bidirectionally coupled model.

3.1 Discretization of the level-set equation

As the level-set equation is defined on the entire unit cell Y, a natural mesh choice is a structured cartesian mesh with step size h, cf. Figure 1. On such a mesh, Finite Difference Methods present themselves as fast and efficient solvers. In the context of level-set equations, the well-known explicit scheme introduced by Rouy and Tourin [34] is used. Although the scheme is first order accurate, it has some favorable properties. It is reported to be more accurate when compared to other first order schemes [41, 55]. The scheme gives numerical solutions fulfilling a discrete maximum principle under reasonable stability restriction on a choice of time steps, see (4). If a smooth enough solution of the level set equation is expected one may use second order schemes as in [16], but we prefer the first order scheme that behaves more stable for example in the situation of discontinuous speed $v_{n,0}$. We note that no so-called reinitialization of the level set function [20, 53, 15] was necessary to apply in our numerical experiments.

The scheme by Rouy and Tourin implements an upwind principle to approximate the spatial derivatives depending on the sign of the interface velocity. In 2D, it can be written as

$$\begin{aligned}L_{ij}^{n+1} = L_{ij}^n - \tau \big(&\max\{v_{n,0}, 0\}\nabla_y^+ L_{ij}^n \\ &+ \min\{v_{n,0}, 0\}\nabla_y^- L_{ij}^n\big)\end{aligned}$$

with

$$\begin{aligned}\nabla_y^+ L_{ij}^n = \big(&\max\{D_{-y_1} L_{ij}^n, -D_{+y_1} L_{ij}^n, 0\}^2 \\ &+ \max\{D_{-y_2} L_{ij}^n, -D_{+y_2} L_{ij}^n, 0\}^2\big)^{\frac{1}{2}}, \\ \nabla_y^- L_{ij}^n = \big(&\max\{-D_{-y_1} L_{ij}^n, D_{+y_1} L_{ij}^n, 0\}^2 \\ &+ \max\{-D_{-y_2} L_{ij}^n, D_{+y_2} L_{ij}^n, 0\}^2\big)^{\frac{1}{2}}.\end{aligned}$$

Here L_{ij}^n denotes an approximation of the level-set $L(t_n, y_{ij})$ at discrete time $t_n := n\tau$ and grid point

y_{ij} of the cartesian mesh. Furthermore, $D_{\pm y_1} L_{ij}^n$ and $D_{\pm y_2} L_{ij}^n$ denote the standard forward and backward differences that approximate the first-order partial derivatives in y_1 and y_2 direction.

With this explicit scheme, a fast treatment of the level-set evolution is possible. As mentioned before a CFL restriction on the time step τ must be fulfilled:

$$\tau \leq \frac{h}{\max |v_{n,0}|}. \tag{4}$$

3.2 Discretization of cell problems

After the nodal values of the level-set function L are computed for the evolved geometry in Y, the effective parameters porosity and specific surface may be computed after a suitable reconstruction of the interface Γ_0. Moreover, the cell problems defined in Theorem 1 must be solved in order to compute the effective diffusion tensor defined in (3). While the structure of the governing equations is fairly simple, a difficulty arises since the fluid domain $Y_{l,0}$ is only defined implicitly by the level-set. Moreover, the boundary conditions are defined on the implicitly given interface Γ_0 which is approximated by the zero contour of the level-set function. One possible approach for a resolution of this issue are front tracking methods. In such methods, the evolved interface is explicitly tracked by introducing new mesh points and discretizing the interface as a lower-dimensional manifold, cf. [48]. Values of new mesh nodes can be obtained via interpolation of the computed nodal values L_{ij}^{n+1}. This, however, produces enormous overhead, as each change of the interface necessarily leads to a reassembly of the computational grid. Furthermore, depending on the topology of the geometry, mesh cells can degenerate and thus invalidate conditions needed for further numerical methods.

Another approach that we apply in this research is based on so-called immersed boundary or interface methods. In these methods the implicitly defined interface is incorporated into the assembly of an existing numerical scheme without any explicit meshing of the interface. As such, we can use a suitable fixed mesh of the unit cell Y for all time steps, and the method shall obtain the current interface position from the nodal values L_{ij}^{n+1}. This approach was used with a great success in multiple scenarios, cf. [19, 21, 27]. One such method that appears convenient for our purposes is the eXtended Finite Element Method (XFEM) [14].

The concept of this method is the enrichment of functions in an existing discrete approximation space of standard FEM by an "enrichment function" ψ [14]. In the case of precipitation and dissolution with one fluid and one solid phase, a natural choice for ψ, that is also used e.g. in [14], is the characteristic function $\mathbb{1}_{Y_{l,0}(t,x)}$ of the fluid phase. This choice simplifies the form of XFEM when applied to the cell problems to compute the effective diffusion tensor (3).

This approach requires an interpolation of the nodal values L_{ij}^{n+1} of the level set function onto the whole unit cell Y. To this end we divide the cartesian mesh as used in the level-set discretization (Section 3.1) into a simplicial mesh, cf. Figure 1. Then, the nodal values L_{ij}^{n+1} on the vertices of the triangles can be uniquely interpolated by a piecewise linear polynomial in each triangle, see also (5) later. This leads to a polygonal interface approximation of Γ_0 represented by the zero level-set of the obtained piecewise linear interpolation. Consequently, each segment of the polygonal interface is a straight line in some triangle T and can be easily reconstructed, cf. Figure 1 for an example of an interface defined by the solution of the level set equation (shown in blue).

We recall some standard notation of the discretization by FEM for our cell problem in the situation that $Y_{l,0} \equiv Y$ using the piecewise linear basis functions φ_k that are associated with all grid points y_{ij}, i.e. $k = k(i,j)$. The numerical solution $\zeta^h(y)$ of the cell problem for $j = 1$ and $j = 2$ is represented in the form

$$\zeta^h(y) = \sum_k \alpha_k \varphi_k(y)\,. \tag{5}$$

The unknown coefficients α_k are determined by solving a system of linear algebraic equations, of which the matrix and the right hand side are assembled from local matrices A^T and right hand sides b^T for each triangle T, namely

$$a_{kl}^T = \int_T \nabla\varphi_k \nabla\varphi_l = |T| \nabla\varphi_k \nabla\varphi_l\,, \tag{6}$$

$$b_k^T = \int_{\partial T \cap \Gamma_0} \nu_0 \cdot e_j \varphi_l = |\partial T \cap \Gamma_0| \nu_0 \cdot e_j \varphi_l(\bar{s}),$$

where $\bar{s}$ is the midpoint of the boundary segment $\partial T \cap \Gamma_0$. Note that in (6) we used also the fact that the gradients $\nabla\varphi_k$ and the normals ν_0 are constant vectors.

Following [14] the eXtended Finite Element Method has to implement the following additional

features when compared to the standard FEM and for $Y_{l,0} \neq Y$. Firstly, all basis functions φ_k (and the associated coefficients α_k) are eliminated from (5) if the support of φ_k lies completely outside of $Y_{l,0}$. Consequently one constructs the system of linear equations only for the unknowns α_k for which the associated grid nodes y_{ij} are vertices of at least one triangle T such that $T \cap Y_{l,0} \neq \emptyset$. Note that such properties can be found easily by checking the signs of the nodal values L_{ij}^{n+1} for each triangle.

Furthermore, if the support of φ_k lies completely in $Y_{l,0}$ then the standard computations as in (6) are used. Finally, one has to modify the computations only for triangles T, for which $T \cap \Gamma_0 \neq \emptyset$ holds, namely

$$a_{kl}^T = |T \cap Y_{l,0}| \nabla \varphi_k \nabla \varphi_l \,,$$
$$b_{j,k}^T = |T \cap \Gamma_0| \nu_0 \cdot e_j \varphi_l(\bar{s}),$$

where $\bar{s}$ is now the midpoint of the (implicitly given) boundary segment $T \cap \Gamma_0$.

With the approach of XFEM, the overhead for the assembly of the stiffness matrix and the right hand side with respect to FEM reduces to the computation of the volumes of all fluid subcells $T \cap Y_{l,0}$ and lengths of all boundary segments $T \cap \Gamma_0$. One has to note that this can increase the condition number of the resulting linear system if the volumes of these fluid subcells are small in comparison to the triangle volumes. Triangles in which this happens (whereby the criterion for "smallness" must be chosen appropriatly) are simply ignored in the assembly routine, cf. Fig. 1.

Having the numerical solutions of the cell problem using the XFEM, we can finally compute the effective diffusion tensor (3) using the same numerical integration as in XFEM.

Finally, the imposed periodic boundary conditions are implemented by a ghost node approach, cf. Fig. 1. Black nodes are used for computations while white nodes are synchronized via periodic boundary conditions and used for e.g. plotting of the level set contours. More precisely, any access to nodes on the upper/right boundary (white circles in Fig. 1) is redirected to the corresponding nodes on the lower/left boundary (black circles in Fig. 1). Rectangular dots represent ghost nodes outside of Y whose values would be needed by the numerical methods.

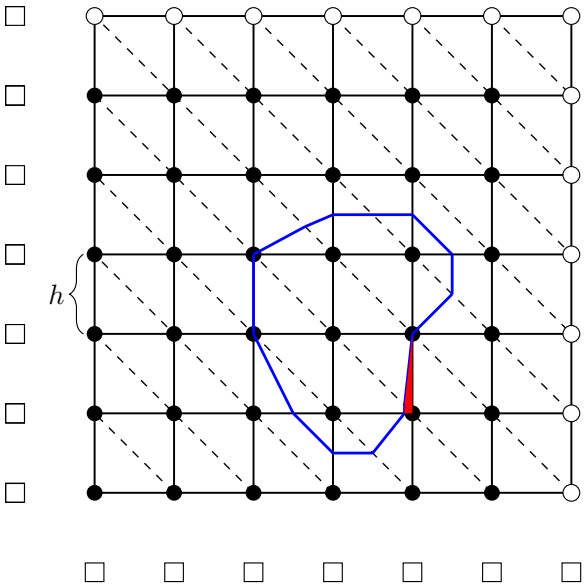

Figure 1: Example mesh of $Y \subset \mathbb{R}^2$. Colors: black: computational nodes, white: periodic boundary/ghost nodes; Shapes: circle: inside of Y, square: ghost nodes outside of Y (not explicitely constructed). Red area: fluid subcells increasing condition number. Bold lines indicate the mesh used for the level-set method, dashed lines are added for the solution of cell problems. Blue lines show a possible interface defined by a level-set function.

3.3 Discretization of macroscopic transport equation and overall solution algorithm

For the solution of the remaining macroscopic problem, we use the MATLAB toolbox HyPHM [12], which provides a parallelized implementation of a solver for flow and transport problems. The underlying discretization of the macroscale transport equation is based on mixed finite elements; more precisely on Raviart-Thomas elements of lowest order [11]. For details, we refer to the manual of [12].

The bidirectional coupling of the macro- and microscale problems is solved algorithmically as illustrated in Figure 2. An operator splitting approach between the two spatial scales offers a simple algorthmic approach to such problems. Such an approach allows combining existing software for simulations of macroscale problems and microscale/level-set problems as well as accurate results. However, the introduction of splitting er-

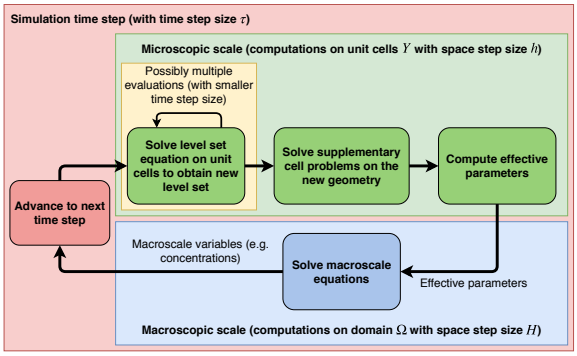

Figure 2: Algorithmic solution for bidirectionally coupled micro-macro problem including evolving microstructures.

rors can impose a heavy penalty on the magnitude of time steps in the simulation and thus can increase computation times. As such, we apply a global implicit handling by means of Newton's method with adaptive time stepping. In such a way, also larger macroscale time steps may be realized which is highly feasible to investigate long-term effects. For this, we apply an algorithm using the Armijo rule in order to increase or decrease time step sizes as needed. However, it often remains necessary to compute multiple microscale time steps for the level-set evolution inside of one time step of the macroscale solver as the macro time step size could violate the CFL restriction (4).

4 Simulation results

In this section, various simulation scenarios with increasing complexity are investigated. We start considering pore-scale examples in the level-set context: First, the clogging of a single pore is investigated (Section 4.1) and second, the dissolution of a mineral composite is considered (Section 4.2). For both scenarios, the impact on bulk transport properties is visualized with focus on their degeneration. Afterwards one sided-coupled micro-macro problems are investigated for both scenarios. More precisely, the outcome of the aforementioned examples is used as an input for the parametrization of a macroscale transport model, cf. Section 4.3. The impact of evolving parameters compared to the case with constant parameters is clearly visible. The bidirectionally coupled micro-macro model is investigated in Section 4.4. As application, the dissolution of a regular array of calcite grains is considered and convergence studies are conducted.

4.1 Clogging of a single pore

In this section, we investigate the clogging of a single pore throat and focus on the degeneration of the related effective diffusion tensor as defined in (3). As geometrical setting, we consider a single pore channel placed in a unit square, cf. left in Figure 3, which is inspired by Li et al. [19, 20]. We investigate precipitation reactions leading to the following constant interface velocity:

$$v_n = \begin{cases} -0.2 & \text{for } |y_1| < 0.15 \\ 0.2 & \text{otherwise} \end{cases}$$

The velocity is extended to the whole domain for computational reasons, cf. right in Figure 3. The computations are realized with $h = \frac{1}{64}$ and $\tau = 0.5h$.

Such a setting leads to the stepwise clogging of the pore throat until the single pore channel is completely filled with the precipitate, cf. right in Figure 3. Consequently, the effective diffusion tensor as defined in (3) degenerates with respect to transport in horizontal direction. This is evident from Figure 4, in which the evolution of the diffusion tensor's eigenvalues is shown. The eigenvalues naturally converge to the eigenvalues corresponding to the limit geometry (dashed green line in Figure 3). From our investigations it is evident that the bulk transport properties significantly change with time and topological changes are easily capable in the level set framework. The impact on macroscopic transport is further studied in Section 4.3.

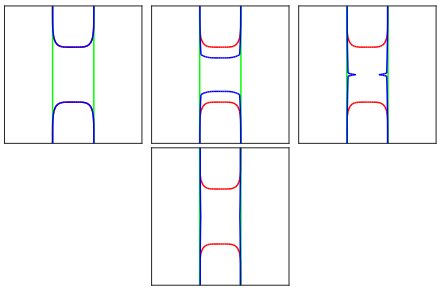

Figure 3: Controlled growth of solid grains by precipitation. Red: initial interface, blue: current interface, green: geometry of pore channel.

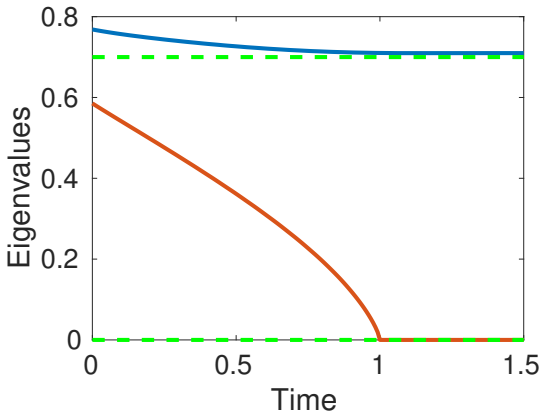

Figure 4: Eigenvalues of the (degenerating) diffusion tensor (red and blue). Eigenvalues of completely clogged pore channel (dashed green) with values 0 and 0.7.

4.2 Dissolution of a mineral composite

Next, we consider the dissolution of a mineral composite similar to the example given in [21]. Two minerals, say calcite and dolomite, form an irregular but periodic pattern left and right to a single pore/fracture, cf. Figure 5 on the left.

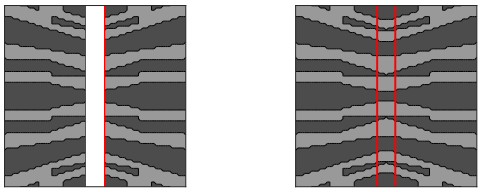

Figure 5: Irregular mineral composition with vertical fracture (left). Definition of dissolution speed $v_{n,\varepsilon}$ extended to the whole domain (right). Calcite (light gray), dolomite (dark grey).

The two minerals are dissolved with different, but constant velocities, cf. Figure 5 on the right:

$$\begin{aligned} v_{n,\text{calcite}} &= 0.5 \\ v_{n,\text{dolomite}} &= 0.05 \end{aligned}$$

The computations are realized on the unit square domain with the discretization steps $h = \frac{1}{80}$ and $\tau = 0.5h$.

It is evident from Figure 6 that the calcite domain is dissolved preferentially and channels/wormholes are formed while dolomite dissolves very slowly and remains as the porous matrix for longer time scales. Consequently, effective diffusion is first possible only in vertical direction (along the fracture) whereas the degenerated eigenvalue corresponding to the horizontal direction becomes positive after reasonable amount of calcite has been dissolved, cf. Figure 7. As in the previous example, bulk transport properties significantly change with time and underlying geometry. The impact on macroscopic transport is again studied in Section 4.3.

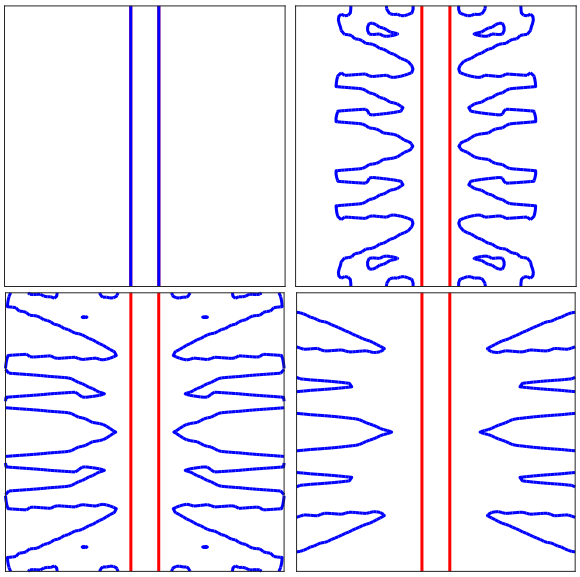

Figure 6: Time series for dissolution of composite of two differently strong dissolvable minerals (calcite and dolomite). Red: initial interface, blue: current interface.

4.3 Simple micro-macro problem

To illustrate the non-negligible effects that the underlying structural evolution of a porous medium has on the macroscale transport behavior, we consider the diffusive transport of a chemical species on a macroscopic domain $\Omega = (0,1)^2$, cf. Section 2:

$$\begin{aligned} \partial_t(\phi c) - \nabla \cdot (\mathbb{D}\nabla c) = 0 \quad &\text{in } (t_0,t_1)\times\Omega, \\ -\mathbb{D}\nabla c \cdot \nu = 0 \quad &\text{on } (t_0,t_1)\times\partial\Omega, \\ c(t_0,x) = \mathbb{1}_{B_r(m)}(x) \quad & \end{aligned}$$

where ϕ and $\mathbb{D}$ are the effective parameters obtained from the microscale, cf. Theorem 1 with $D = 0.01$. The initial values are depicted on the top in Figure 8 and 9 and given by the charac-

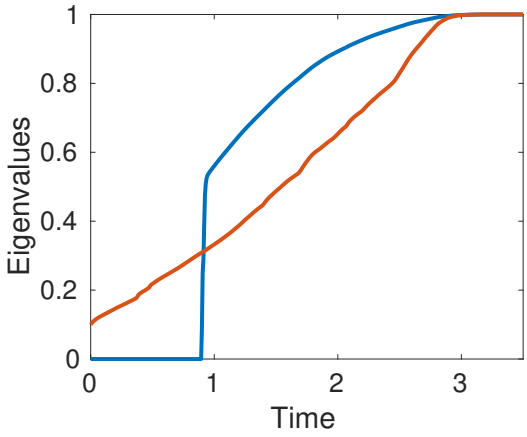

Figure 7: Eigenvalues of the (degenerating) diffusion tensor.

teristic function $\mathbb{1}_{B_r(m)}$ of the circle with radius $r = 0.15$ around the midpoint $m = (0.5, 0.5)^T$ of Ω, i.e.

$$\mathbb{1}_{B_r(m)}(x) = \begin{cases} 1, & \|x - m\| < r, \\ 0, & \text{otherwise.} \end{cases}$$

For the evolution of the fluid-solid interface at the microscale we consider the scenarios described in Sections 4.1 and 4.2. Consequently, the values computed there are taken for the parametrization of the macroscopic transport equation. In this sense, we evaluate a one-sided coupled micro-macro problem since the macroscale solution has not back coupling to the microscale problem. Moreover, the cell problems vary in time but not in space, i.e. only one cell problem and the corresponding values of ϕ and $\mathbb{D}$ have to be evaluated per time step which significantly reduces the computational burden. For both scenarios we evaluate the following three test cases:

1. Effective parameters are fixed at the initial time (the values at $t = 0$ for the single pore scenario, the values at $t = 0.90625$ for the mineral dissolution scenario).
2. Effective parameters vary in time dependent on the current state of the underlying geometry
3. Effective parameters are fixed at values obtained in the time $t = 1.5$.

Note that numerically stable simulations are only possible for symmetric and positive definite diffusion tensors $\mathbb{D}$ within the used software package HyPHM, i.e. for time intervals $(t_0, t_1) \subset (0, 1.5)$ in which the diffusion tensors do not degenerate, cf. Figure 4 and 7. Numerical tests showed that with our chosen time step size of 0.00625, the largest usable time interval without numerical instabilities is $(0, 0.99375)$ in the pore clogging scenario. In the mineral dissolution scenario, numerical tests showed that $(0.90625, 1.5)$ is the largest usable time interval without numerical instabilities.

It is evident from the simulation outcome depicted in Figure 8 and 9 that the choice of a constant parametrization shows significantly different behavior than the choice of a dynamic parametrization. This is particularly the case if transport is restricted to one spatial direction, cf. Figure 8 on the right and Figure 9 on the left. We conclude that changes in pore-scale structures are non-negligible for accurate macroscopic model description, especially if degeneration of transport to one spatial direction plays a role.

4.4 Advanced micro-macro problem

In this section, we investigate the bidirectionally coupled micro-macro problem and proof the capability of our model approach. The various couplings inherent to this problem are illustrated in Figure 2. We consider the dissolution of an array of calcite grains similar to [22] who investigated the same scenario, but in the context of a pore-scale simulations. At the pore scale, the domain $\Omega = (0, 1) \times (0, 0.5)$ [cm^2] is filled with equally distributed calcite grains with an initial radius of 0.01 cm (28 slices with 13 or 14 grains in each slices). These grains are dissolved by surface reactions through the following pathways [46]

$$\mathrm{CaCO_{3(s)}} \rightarrow \mathrm{Ca^{2+}} + \mathrm{CO_3^{2-}}$$
$$\mathrm{CaCO_{3(s)}} + \mathrm{H^+} \rightarrow \mathrm{Ca^{2+}} + \mathrm{HCO_3^-}$$

into calcium and (hydrogen)carbonate. The surface reaction rate of this pathway is

$$R(\vec{c}) = (k_1 c_{\mathrm{H^+}} + k_3) \left(1 - \frac{c_{\mathrm{Ca^{2+}}} c_{\mathrm{CO_3^{2-}}}}{K_{\mathrm{eq}}}\right) \text{[mol m}^{-2}\text{s}^{-1}\text{]} \tag{7}$$

with rate constants $k_1 = 0.89$[mol m^{-2} s^{-1}], $k_3 = 6.6 \cdot 10^{-7}$[mol m^{-2} s^{-1}] and equilibrium constant $K_{\mathrm{eq}} = 10^{-8.234}$.

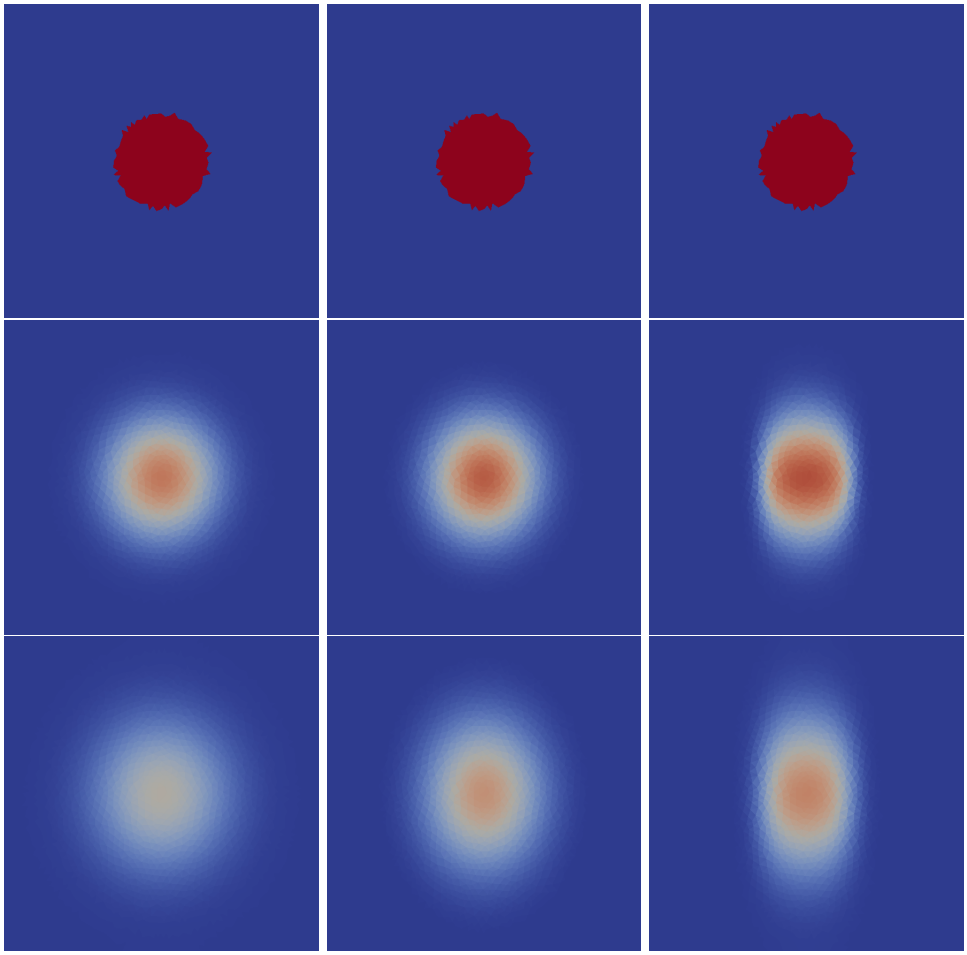

Figure 8: Diffusion of macroscopic concentration in the pore clogging scenario. Each column shows the simulations of the test cases 1 to 3. From top to bottom: solutions at $t = 0$, $t = 0.5$ and $t = 0.96875$. All images are taken with a linear scale from 0 to 1.

We are interested in investigations at the macroscopic scale and the setting transfers to the following macroscopic reactive transport problem in the domain Ω for the vector of mobile species $\vec{c} = (c_{H^+}, c_{Ca^{2+}}, c_{CO_3^{2-}})$, cf. Section 2.

$$
\begin{aligned}
\partial_t(\phi\vec{c}) + \mathcal{L}\vec{c} &= 28\sigma\vec{R}(\vec{c}) \quad \text{in } \Omega, \qquad (8)\\
(\mathcal{L}\vec{c})_* &:= \nabla\cdot(c_*\vec{v} - \mathbb{D}\nabla c_*)\,,\\
&\quad * \in \{H^+, Ca^{2+}, CO_3^{2-}\},\\
(c_*\vec{v} - \mathbb{D}\nabla c_*)\cdot\vec{n} &= 0 \quad \text{on } (0,1)\times\{0, 0.5\},\\
(c_{Ca^{2+}}\vec{v} - \mathbb{D}\nabla c_{Ca^{2+}})\cdot\vec{n} &= 0 \quad \text{on } \{0\}\times(0, 0.5),\\
(c_{CO_3^{2+}}\vec{v} - \mathbb{D}\nabla c_{CO_3^{2+}})\cdot\vec{n} &= 0 \quad \text{on } \{0\}\times(0, 0.5),\\
(c_{H^+}\vec{v} - \mathbb{D}\nabla c_{H^+})\cdot\vec{n} &= 10^{-5}\vec{v}\cdot\vec{n}\\
&\quad \text{on } \{0\}\times(0, 0.5),\\
-\mathbb{D}\nabla c_*\cdot\vec{n} &= 0 \quad \text{on } \{1\}\times(0, 0.5),\\
c_{Ca^{2+}}(0,\cdot) &= 0,\\
c_{CO_3^{2+}}(0,\cdot) &= 0,\\
c_{H^+}(0,\cdot) &= 10^{-5},
\end{aligned}
\qquad (9)
$$

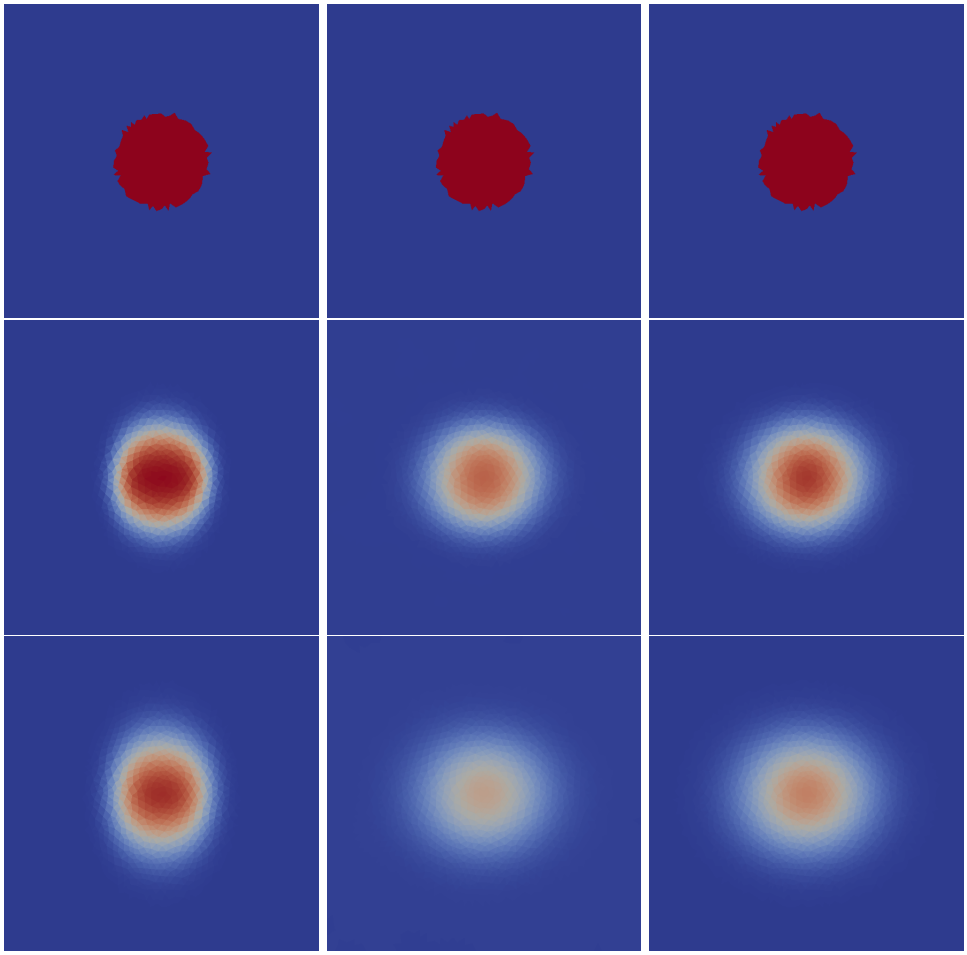

Figure 9: Diffusion of macroscopic concentration in the mineral dissolution scenario. Each column shows the simulations of the test cases 1 to 3. From top to bottom: solutions at $t = 0.90625$, $t = 1.2$ and $t = 1.5$. All images are taken with a linear scale from 0 to 1.

with porosity ϕ, specific surface σ, and effective diffusion tensor $\mathbb{D}$ as defined in (3) with molecular diffusion coefficient $D = \frac{1}{50000}[\mathrm{cm}^2\ \mathrm{s}^{-1}]$. The vector $\vec{R}$ of reaction rates is given by

$$\vec{R}\,(\vec{c}) := \begin{pmatrix} -k_1 c_{\mathrm{H}^+}\left(1 - \frac{c_{\mathrm{Ca}^{2+}} c_{\mathrm{CO}_3^{2-}}}{K_{\mathrm{eq}}}\right) \\ R(\vec{c}) \\ R(\vec{c}) \end{pmatrix}$$

with the reaction rate R from (7).

The geometry of the domain Y on which the cell problems are defined is determined by the level set equation

$$\partial_t L + v_n |\nabla L| = 0 \qquad \text{in } \Omega \times Y$$

with $Y = [-\frac{1}{2}, \frac{1}{2}]^2$ and initial level set $L^0(\vec{y}) = 0.28 - |\vec{y}|$. This initial state is chosen for all $\vec{x} \in \Omega$.

We consider the following two situation: First, the isotropic situation, for which we assume that uniform dissolution takes place and that the normal velocity of the interface v_n is related to the reaction rate $R(\vec{c})$, cf. Section 4.4.1. Second, the anisotropic situation, for which we additionally incorporate the impact the direction of flow has on the dissolution profile and therefore modulate the relation of the isotropic situation by means of a function f, cf. Section 4.4.2.

In both situations, the dissolution speed depends on the macroscopic concentrations of the mobile species hygrogen H^+, calcite Ca^{2+}, carbonate CO_3^{2-}, and hydrogen carbonate HCO_3^- and thus varies throughout the macroscopic domain. However, in the case of uniform or compact dissolution a vertically uniform dissolution speed is expected, whereas along the horizontal axis a hetero-

geneous distribution is evident due to a prescribed uniform advective flux. We consider two velocities, $\vec{v} = 0.1 \cdot (1,0)^T$[cm s^{-1}] and $\vec{v} = 0.001 \cdot (1,0)^T$[cm s^{-1}], resulting in Peclet numbers of 5000 and 50, respectively.

Consequently, we decompose the macroscopic domain in vertical slices, cf. Figure 14. A distinct constant concentration value is obtained for each slice by averaging the respective values over the slice. For each such slice, the level set evolution must be evaluated in a representative unit cell Y.

In the situation described in [22], a pore-scale simulation based on 28 physical slices is considered. In the micro-macro context, this results in the computation of $28 \cdot N$ level-set evolution steps (where $N \in \mathbb{N}$ is a fixed number of level-set evolutions for every cell problem) and assemble and solve 28 linear systems for the discretization of the cell problems. In our simulations, we set $N = 10$ in order to ensure a sufficient accuracy of the solution of the level-set equation. As the computational time for the level-set equation is small in comparison to solving the cell problems, even a larger choice for N causes no significant simulation overhead.

4.4.1 Isotropic situation

In the isotropic situation, the normal velocity of the interface v_n is related to the reaction rate via

$$v_n = 28 V_m R(\vec{c})[(\text{length scale of Y})\text{s}^{-1}] \qquad (10)$$

with molar volume of calcite $V_m = 36.93$[cm^3 mol^{-1}] [10].

In Figure 10 and 11 the resulting uniform dissolution of calcite grains in the unit cell Y are depicted from which macroscopic transport properties are calculated. Figure 12 shows the macroscopic calcium concentration at final time for the situation of 28 slices as described in [22] with $Pe = 50$ and $Pe = 5000$. The range of concentration obtained in the micro-macro context perfectly fits the ones of the pore-scale simulations conducted in [22].

Ultimately, we study the convergence properties of our solution scheme as summarized in Tables 1 to 5 to quantify the effort of the micro-macro approach. To estimate a so-called Experimental Order of Convergence (the EOC) with respect to some discretization parameter, e.g. H, h, or ε, we compute a series of examples in which one of this discretization parameter is refined uniformly by a factor of 2, e.g., H_0 is given and $H_{j+1} = 0.5 H_j$, $j \in \mathbb{N}$ and

$$EOC \approx \log_2 \left(\frac{\|c_j - c_{j+1}\|}{\|c_{j+1} - c_{j+2}\|} \right), \qquad (11)$$

where c_j denotes the obtained calcium concentration for the j-th value of the discretization parameter.

We first investigate the approximation quality of the macroscopic transport for various numbers of slices, i.e. the computational domain is virtually represented by a different number of slices $N \in \{25, 50, 100, 200, 400\}$, cf. Figure 14. In doing so, the right hand side of (8) and (10) must

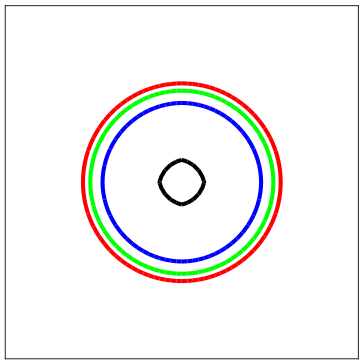

Figure 10: Fluid–solid interface at initial time for all slices (red) and at time T for leftmost slice (black), middle slice (blue), and rightmost slice (green).

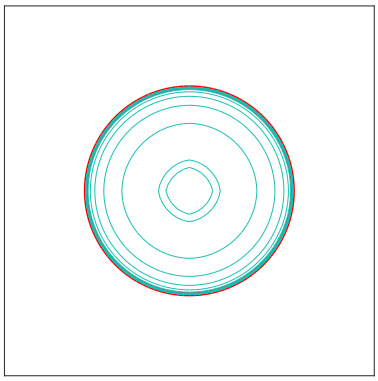

Figure 11: Evolution of the interface on the leftmost slice with nonequidistant time step sizes.

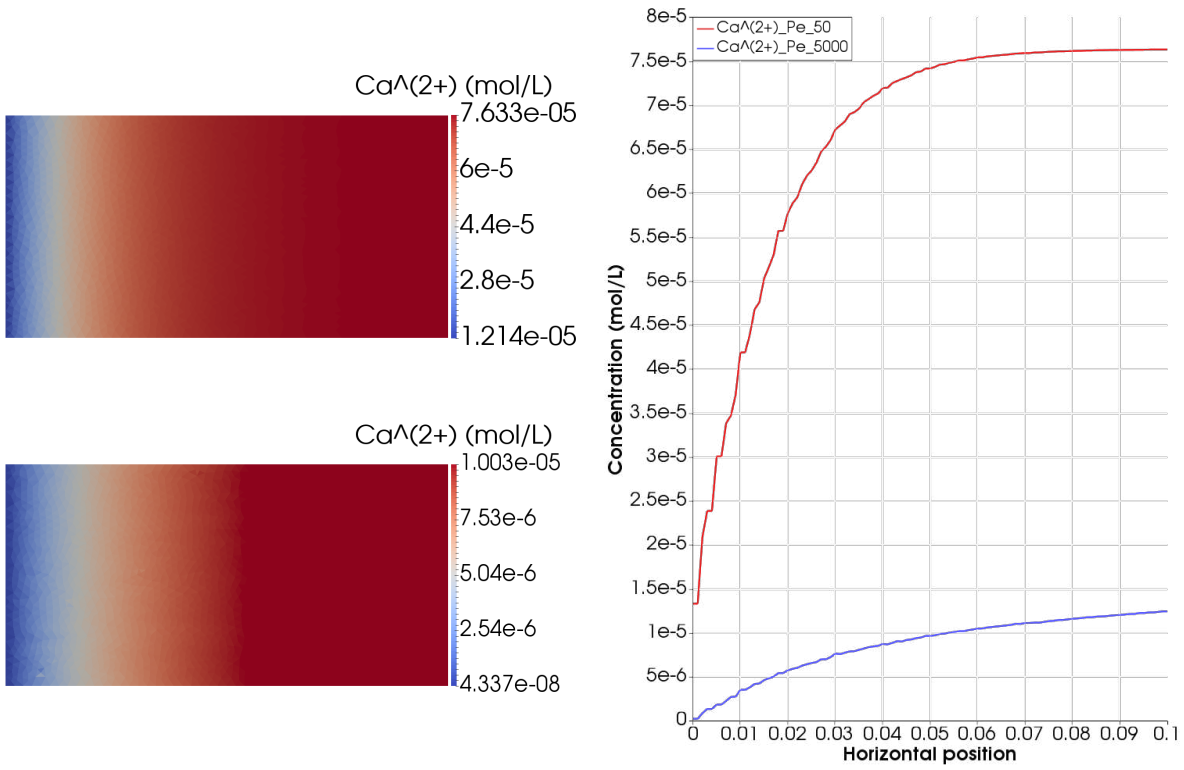

Figure 12: Macroscopic calcium concentrations for different Peclet numbers. Top left: Pe = 50, bottom left: Pe = 5000. Right: 1D comparison of values.

be replaced by $\frac{1}{\varepsilon}\sigma\vec{R}(\vec{c})$ and $\frac{1}{\varepsilon}V_m R(\vec{c})$ with scaling parameter $\varepsilon := \frac{1}{N}$. In Figure 12 the horizontal distribution of Ca^{2+} is shown and in Table 1 the EOC is evaluated depending on the number of slices.

For the refinement of the macroscopic discretization parameter H, we fix the values $h = 1/64$ and $\varepsilon = 1/50$ and consider $Pe = 50$ and $Pe = 5000$. We obtain the EOC being 1, cf. Tables 2 and 4. This confirms the expected order of convergence of the mixed FEM with P_0-RT_0 elements.

For the refinement of the microscopic discretization parameter h while choosing $H = \frac{1}{500}$ and $\varepsilon = \frac{1}{50}$, our simulations using Newton's method for a globally implicit handling show an estimated order of convergence of 2, cf. Tables 3 and 5. The results show that the orders of convergence stay the same for $Pe = 5000$ and $Pe = 50$. However, for smaller Peclet number we obtain "smoother" values for the order of convergence. A possible explanation lies in the effect of the time discretization. In the globally implicit approach, we choose a non-equidistant time step size. This is neccessary as the initial values lead to instabilities due to nonconformity with the reactive system. After the initial stage of the simulation, the system stays stable even with larger time step sizes. This allows for a speedup of total simulation time. This can imply that the time discretization error becomes dominant with time, which could be seen in the case of large velocities.

4.4.2 Anisotropic situation

In this Section, we consider the more sophisticated anisotropic scenario. In this scenario, we include the impact that the direction of flow has on the dissolution profile. More precisely, the angle between fluid velocity and outer normal of the fluid (i.e. pointing into the solid) is included into the dissolution rate. In this sense an anisotropic geometry evolves even when starting with an isotropic initial geometry, cf. Figure 17. In such situations it is crucial to apply the level set solver to resolve the evolution of the geometry. The previous example could also be handled using a representative radial formulation as in [11].

In order to observe effects of fluid flow on the evolution of the fluid-solid-interface in the mi-

Table 1: Errors and estimated order of convergence wrt. scale separation factor ε. Other parameters: Pe $= 5000$, $H = 1/1000$, $h = 1/64$.

ε	$\|c_{\varepsilon_{i-1}} - c_{\varepsilon_i}\|_{L^2}$	$\frac{\|c_{\varepsilon_{i-1}} - c_{\varepsilon_i}\|_{L^2}}{\|c_{\varepsilon_i}\|_{L^2}}$	EOC (L^2)	$\|c_{\varepsilon_{i-1}} - c_{\varepsilon_i}\|_{L^1}$	$\frac{\|c_{\varepsilon_{i-1}} - c_{\varepsilon_i}\|_{L^1}}{\|c_{\varepsilon_i}\|_{L^1}}$	EOC (L^1)
$\frac{1}{25}$	-	-	-	-	-	-
$\frac{1}{50}$	5.7105e−9	1.7533e−2	-	3.6233e−10	1.7987e−2	-
$\frac{1}{100}$	1.8578e−9	5.7310e−3	1.6200	1.2409e−10	6.1985e−3	1.5459
$\frac{1}{200}$	4.1242e−10	1.2736e−3	2.1714	2.7048e−11	1.3529e−3	2.1978
$\frac{1}{400}$	6.9247e−11	2.1386e−4	2.5743	3.9231e−12	1.9625e−4	2.7855

Table 2: Errors and estimated order of convergence wrt. macroscale discretization parameter H with Newton after implementation of non-equidistant time steps. Other parameters: Pe $= 5000$, $h = 1/64$, $\varepsilon = 1/50$

H	$\|c_{H_{i-1}} - c_{H_i}\|_{L^2}$	$\frac{\|c_{H_{i-1}} - c_{H_i}\|_{L^2}}{\|c_{H_i}\|_{L^2}}$	EOC (L^2)	$\|c_{H_{i-1}} - c_{H_i}\|_{L^1}$	$\frac{\|c_{H_{i-1}} - c_{H_i}\|_{L^1}}{\|c_{H_i}\|_{L^1}}$	EOC (L^1)
$\frac{1}{50}$	-	-	-	-	-	-
$\frac{1}{100}$	5.7332e−8	8.1628e−2	-	2.5411e−9	5.4319e−2	-
$\frac{1}{200}$	3.8718e−8	5.5215e−2	0.5664	1.5330e−9	3.2843e−2	0.7290
$\frac{1}{400}$	1.3844e−8	1.9741e−2	1.4837	6.2588e−10	1.3411e−2	1.2924
$\frac{1}{800}$	7.9131e−9	1.1284e−2	0.8070	3.4007e−10	7.2868e−3	0.8801

Table 3: Errors and estimated order of convergence wrt. microscale discretization parameter h with Newton after implementation of non-equidistant time steps. Other parameters: Pe $= 5000$, $H = 1/500$, $\varepsilon = 1/50$

h	$\|c_{h_{i-1}} - c_{h_i}\|_{L^2}$	$\frac{\|c_{h_{i-1}} - c_{h_i}\|_{L^2}}{\|c_{h_i}\|_{L^2}}$	EOC (L^2)	$\|c_{h_{i-1}} - c_{h_i}\|_{L^1}$	$\frac{\|c_{h_{i-1}} - c_{h_i}\|_{L^1}}{\|c_{h_i}\|_{L^1}}$	EOC (L^1)
$\frac{1}{4}$	-	-	-	-	-	-
$\frac{1}{8}$	1.1911e−8	1.7044e−2	-	7.6489e−10	1.6452e−2	-
$\frac{1}{16}$	6.7455e−9	9.6267e−3	0.8204	2.0190e−10	4.3301e−3	1.9216
$\frac{1}{32}$	9.7455e−10	1.3899e−3	2.7911	4.0284e−11	8.6334e−4	2.3254
$\frac{1}{64}$	2.0741e−10	2.9576e−4	2.2322	9.6652e−12	2.0710e−4	2.0593

Table 4: Errors and estimated order of convergence wrt. macroscale discretization parameter H with Newton after implementation of non-equidistant time steps. Other parameters: Pe = 50, $h = 1/64$, $\varepsilon = 1/50$

H	$\|c_{H_{i-1}} - c_{H_i}\|_{L^2}$	$\frac{\|c_{H_{i-1}} - c_{H_i}\|_{L^2}}{\|c_{H_i}\|_{L^2}}$	EOC (L^2)	$\|c_{H_{i-1}} - c_{H_i}\|_{L^1}$	$\frac{\|c_{H_{i-1}} - c_{H_i}\|_{L^1}}{\|c_{H_i}\|_{L^1}}$	EOC (L^1)
$\frac{1}{50}$	-	-	-	-	-	-
$\frac{1}{100}$	3.0811e−7	6.3944e−2	-	1.0945e−8	3.2965e−2	-
$\frac{1}{200}$	1.5989e−7	3.3182e−2	0.9464	5.3837e−9	1.6222e−2	1.0236
$\frac{1}{400}$	8.1146e−8	1.6841e−2	0.9785	2.6630e−9	8.0253e−3	1.0156
$\frac{1}{800}$	4.0878e−8	8.4838e−3	0.9892	1.3232e−9	3.9878e−3	1.0090

Table 5: Errors and estimated order of convergence wrt. microscale discretization parameter h with Newton after implementation of non-equidistant time steps. Other parameters: Pe = 50, $H = 1/500$, $\varepsilon = 1/50$

h	$\|c_{h_{i-1}} - c_{h_i}\|_{L^2}$	$\frac{\|c_{h_{i-1}} - c_{h_i}\|_{L^2}}{\|c_{h_i}\|_{L^2}}$	EOC (L^2)	$\|c_{h_{i-1}} - c_{h_i}\|_{L^1}$	$\frac{\|c_{h_{i-1}} - c_{h_i}\|_{L^1}}{\|c_{h_i}\|_{L^1}}$	EOC (L^1)
$\frac{1}{4}$	-	-	-	-	-	-
$\frac{1}{8}$	3.6953e−8	7.6783e−3	-	1.9739e−9	5.9568e−3	-
$\frac{1}{16}$	6.5488e−9	1.3595e−3	2.4964	3.4800e−10	1.0491e−3	2.5039
$\frac{1}{32}$	1.6138e−9	3.3494e−4	2.0208	8.5591e−10	2.5796e−4	2.0235
$\frac{1}{64}$	4.0384e−10	8.3811e−5	1.9986	2.1405e−11	6.4510e−5	1.9995

croscale, we consider a variable normal velocity:

$$v_n(\vec{c},\vec{v}) := v_{\text{n,iso}}(\vec{c}) f(\vec{v}\cdot\vec{n}),$$
$$f(x) := \begin{cases} \exp(-\mu x^2), & x \le 0, \\ (1-\lambda)\exp(-\mu x^2) + \lambda, & x > 0, \end{cases} \tag{12}$$

with parameters $\mu > 0$, $0 \le \lambda \le 1$. For $f = 1$, we exactly obtain the normal velocity $v_{\text{n,iso}}$ as given in (10). The function f modulates the solid dissolution depending on magnitude of the velocity and the angle α enclosed with the boundary since $\vec{v}\cdot\vec{n} = |\vec{v}|\cos(\alpha)$. Positive values of $\vec{v}\cdot\vec{n}$ correspond to an acute angle, i.e. the left part of the solid grains which is first hit by an fluid inflowing from left to right. Likewise, negative values of $\vec{v}\cdot\vec{n}$ correspond to an obtuse angle, i.e. the right part of the solid which is in its slipstream. Since the fluid flow transports the reacting chemicals to the solid, the function f takes larger values for $\vec{v}\cdot\vec{n}$ positive than for $\vec{v}\cdot\vec{n}$ negative. The maximum value of f around $\vec{v}\cdot\vec{n} = 0$, $\alpha = 90°$ models the effect that dissolution happens the fastest in regions where the reaction product (dissolved calcium) is transported away quickly (top and bottom of the grain). On the contrary, the value of f is minimal directly behind the grain, i.e. for $\alpha = 180°$.

The inflection point of (12) lies at $x = \frac{1}{(\sqrt{2}\mu)}$. As a consequence, the order of magnitude of μ is a critical choice in order to obtain a suitable geometry. Figure 15 shows plots of f given in (12) for different values for μ. Figure 17 depicts the resulting evolving microscopic geometries for these choices. It is evident that the choice μ = 5e+2 reproduces the nearly isotopic behavior which was already studied in Section 4.4.1 since f is close to 1. The value μ = 5e+4 leads to the following dissolution behavior. For acute angles, an almost uniform dissolution speed is seen, while for obtuse angles, there is almost no dissolution. The value μ = 5e+3 reproduce shapes as they have also been observed in [22] and seems to be a reasonable choice. For this parameter, convergence tests for the fully coupled micro-macro problem with non-uniformly evolving geometry as performed for the isotropic setting in Section 4.4.1 have been carried out. The results are shown in Tables 6, 7, 8, and 9.

The estimated order of convergence (EOC) is 1 in the macroscopic as well as in the microscopic discretization parameters H and h. The EOC in the macroscopic parameter H does not change compared to the scenario investigated in Section 4.4. However, the EOC in the microscopic parameter h reduces from 2 to 1. As a first-order scheme is used for the discretization of the level set equation, this order of convergence is to be expected. The difference between this scenario and section 4.4 lies in the anisotropic evolution of the solid grains. We conclude that the higher EOC in

Table 6: Errors and estimated order of convergence wrt. macroscale discretization parameter H with Newton after implementation of non-equidistant time steps. Other parameters: Pe = 5000, $h = 1/64$, $\varepsilon = 1/50$

H	$\|c_{H_{i-1}} - c_{H_i}\|_{L^2}$	$\frac{\|c_{H_{i-1}} - c_{H_i}\|_{L^2}}{\|c_{H_i}\|_{L^2}}$	EOC (L^2)	$\|c_{H_{i-1}} - c_{H_i}\|_{L^1}$	$\frac{\|c_{H_{i-1}} - c_{H_i}\|_{L^1}}{\|c_{H_i}\|_{L^1}}$	EOC (L^1)
$\frac{1}{50}$	-	-	-	-	-	-
$\frac{1}{100}$	2.1690e−7	4.5028e−1	-	1.4790e−8	4.7870e−1	-
$\frac{1}{200}$	2.2991e−8	4.8529e−2	3.2379	1.1961e−9	3.9565e−2	3.6282
$\frac{1}{400}$	9.6600e−9	2.0452e−2	1.2510	5.2020e−10	1.7275e−2	1.2012
$\frac{1}{800}$	5.8865e−9	1.2474e−2	0.7146	2.7957e−10	9.2918e−3	0.8959

Table 7: Errors and estimated order of convergence wrt. microscale discretization parameter h with Newton after implementation of non-equidistant time steps. Other parameters: Pe = 5000, $H = 1/500$, $\varepsilon = 1/50$

h	$\|c_{h_{i-1}} - c_{h_i}\|_{L^2}$	$\frac{\|c_{h_{i-1}} - c_{h_i}\|_{L^2}}{\|c_{h_i}\|_{L^2}}$	EOC (L^2)	$\|c_{h_{i-1}} - c_{h_i}\|_{L^1}$	$\frac{\|c_{h_{i-1}} - c_{h_i}\|_{L^1}}{\|c_{h_i}\|_{L^1}}$	EOC (L^1)
$\frac{1}{4}$	-	-	-	-	-	-
$\frac{1}{8}$	8.3149e−8	2.0246e−1	-	4.7693e−9	1.8716e−1	-
$\frac{1}{16}$	6.5394e−8	1.4647e−1	0.3465	3.1172e−9	1.1029e−1	0.6135
$\frac{1}{32}$	1.8606e−8	4.0092e−2	1.8134	1.2595e−9	4.2662e−2	1.3074
$\frac{1}{64}$	9.4874e−9	2.0103e−2	0.9717	5.7432e−10	1.9091e−2	1.1329

section 4.4 is a sign of superconvergence resulting from the regular structure of the geometry.

5 Conclusion

In this research, we presented an overall solution strategy for efficiently solving fully coupled micro-macro problems which are the result of an averaging procedure. For illustration purposes, we focused on problems including dynamically evolving microstructures as a result of precipitation and dissolution reactions. In order to capture the arising interfaces explicitly, the problem was implemented in a level-set framework. This present research was designed to demonstrate feasiblity of fully coupled micro-macro models. Despite their complexity, suitable numerical tools have been applied to overcome the computational burden. This proof of concept is of highly practical relevance since micro-macro problems can captured the physics of the porous media applications in great detail. However, further research is needed to improve the accuracy of the model description and simulation results. A well-known improvement for avoiding negative concentrations and accounting for the constant activity of minerals is the modeling of dissolution/precipitation reactions by means of a set valued Heavyside graph [6]. Moreover, it seems reasonable to apply a Mixed Finite Element discretization for the cell problems in order to avoid numerical differentiation. Finally, further research might certainly include the detailed aspects of non-constant fluid flow, e.g. by means of Darcy's law and related auxiliary cell problems. It is to be expected that the same methods applied in this research are directly transferable to the additional model components. This research's solution strategies and findings are helpful when further exploring fully coupled micro-macro problems such as in the field of biofilm growth.

In our research, representatives of realistic pore scale geometries have already been used. An important issue that is a topic of current discussions and needs further evaluation is investigating of the accuracy of upscaled quantities at various scales, i.e. for various sizes of realistic representative elementary volumes. Our findings may be used to study this impact on macroscale transport behavior in porous media and helps balancing the need for accurate bulk parameters versus computational effort.

Acknowledgements

This research was kindly supported by the women's prize of the faculty of natural sciences 2016, Friedrich-Alexander Universität Erlangen-Nürnberg and the DFG Research Training Group 2339 Interfaces, Complex Structures, and Singular

Table 8: Errors and estimated order of convergence wrt. macroscale discretization parameter H with Newton after implementation of non-equidistant time steps. Other parameters: Pe = 50, $h = 1/64$, $\varepsilon = 1/50$

H	$\|c_{H_{i-1}} - c_{H_i}\|_{L^2}$	$\frac{\|c_{H_{i-1}} - c_{H_i}\|_{L^2}}{\|c_{H_i}\|_{L^2}}$	EOC (L^2)	$\|c_{H_{i-1}} - c_{H_i}\|_{L^1}$	$\frac{\|c_{H_{i-1}} - c_{H_i}\|_{L^1}}{\|c_{H_i}\|_{L^1}}$	EOC (L^1)
$\frac{1}{50}$	-	-	-	-	-	-
$\frac{1}{100}$	3.1951e−7	6.7237e−2	-	1.1671e−8	3.5746e−2	-
$\frac{1}{200}$	1.5244e−7	3.2111e−2	1.0676	5.4398e−9	1.6695e−2	1.1014
$\frac{1}{400}$	7.6805e−8	1.6171e−2	0.9889	2.6732e−9	8.2004e−3	1.0250
$\frac{1}{800}$	3.8704e−8	8.1491e−3	0.9887	1.3270e−9	4.0707e−3	1.104

Table 9: Errors and estimated order of convergence wrt. microscale discretization parameter h with Newton after implementation of non-equidistant time steps. Other parameters: Pe = 50, $H = 1/500$, $\varepsilon = 1/50$

h	$\|c_{h_{i-1}} - c_{h_i}\|_{L^2}$	$\frac{\|c_{h_{i-1}} - c_{h_i}\|_{L^2}}{\|c_{h_i}\|_{L^2}}$	EOC (L^2)	$\|c_{h_{i-1}} - c_{h_i}\|_{L^1}$	$\frac{\|c_{h_{i-1}} - c_{h_i}\|_{L^1}}{\|c_{h_i}\|_{L^1}}$	EOC (L^1)
$\frac{1}{4}$	-	-	-	-	-	-
$\frac{1}{8}$	5.0855e−8	1.0742e−2	-	2.7857e−9	8.5787e−3	-
$\frac{1}{16}$	1.4653e−8	3.0888e−3	1.7952	7.7583e−10	2.3835e−3	1.8442
$\frac{1}{32}$	5.1457e−9	1.0840e−3	1.5097	2.6772e−10	8.2182e−4	1.5350
$\frac{1}{64}$	2.0875e−9	4.3965e−4	1.3016	1.0721e−10	3.2899e−4	1.3203

Limits. We further acknowledge the helpful discussions with Florian Frank who also provided his toolbox HyPHM. The third author was supported by VEGA 1/0709/19 and APVV-15-0522.

References

[1] Battiato, I., Tartakovsky, D.M., Tartakovsky, A.M., Scheibe, T.: On breakdown of macroscopic models of mixing-controlled heterogeneous reactions in porous media. Advances in water resources **32**(11), 1664–1673 (2009)

[2] Battiato, I., Tartakovsky, D.M., Tartakovsky, A.M., Scheibe, T.D.: Hybrid models of reactive transport in porous and fractured media. Advances in Water Resources **34**(9), 1140–1150 (2011)

[3] Bensoussan, A., Lions, J.L., Papanicolaou, G.: Asymptotic analysis for periodic structures, vol. 374. American Mathematical Soc. (2011)

[4] Blunt, M.J., Bijeljic, B., Dong, H., Gharbi, O., Iglauer, S., Mostaghimi, P., Paluszny, A., Pentland, C.: Pore-scale imaging and modelling. Advances in Water Resources **51**, 197–216 (2013)

[5] Daly, K.R., Roose, T.: Homogenization of two fluid flow in porous media. Proceedings of the Royal Society A: Mathematical, Physical and Engineering Sciences **471**(2176), 20140564 (2015)

[6] van Duijn, C.J., Knabner, P.: Crystal dissolution in porous media flow. Journal of Applied Mathematics and Mechanics **76**, 329332 (1996). URL http://www.mso.math.fau.de/fileadmin/am1/users/knabner/publicationen/CrystalDiss__.pdf

[7] Ebigbo, A., Helmig, R., Cunningham, A.B., Class, H., Gerlach, R.: Modelling biofilm growth in the presence of carbon dioxide and water flow in the subsurface. Advances in Water Resources **33**(7), 762–781 (2010)

[8] Eck, C.: Analysis of a two-scale phase field model for liquid-solid phase transitions with equiaxed dendritic microstructure. Multiscale Modeling & Simulation **3**(1), 28–49 (2005)

[9] Ellis, B., Peters, C., Fitts, J., Bromhal, G., McIntyre, D., Warzinski, R., Rosenbaum, E.: Deterioration of a fractured carbonate caprock exposed to co2-acidified brine flow. Greenhouse Gases: Science and Technology **1**(3), 248–260 (2011)

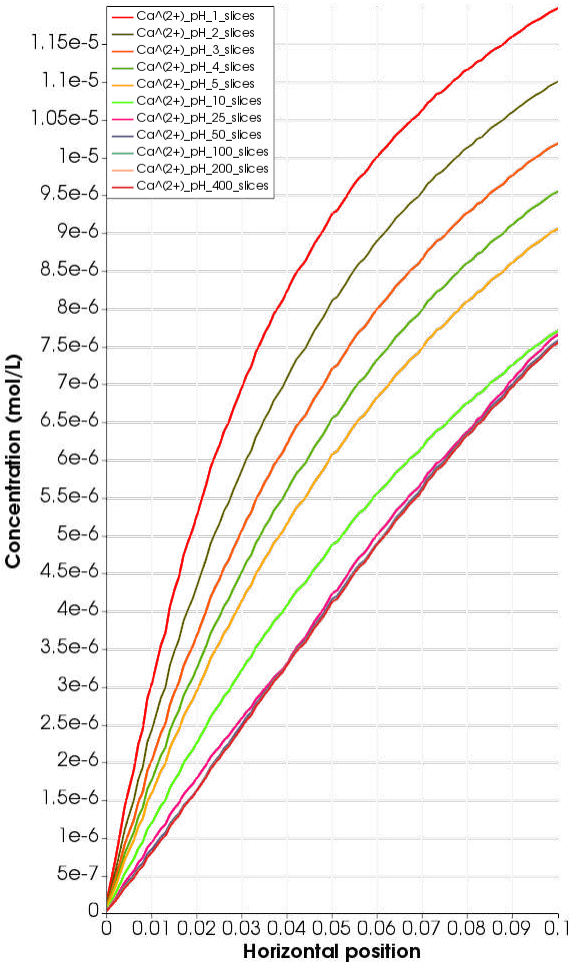

Figure 13: Distribution of calcium concentration $c_{Ca^{2+}}$ alongside the horizontal dimension of Ω for different numbers of slices.

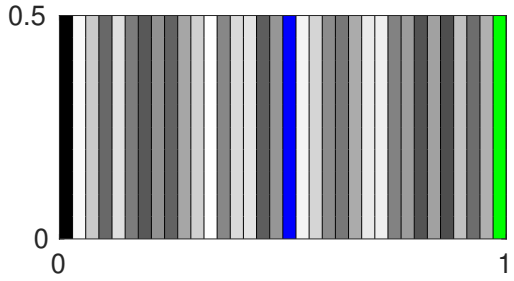

Figure 14: Partition of macroscopic domain Ω into vertical slices. Each slice is colored differently in order to highlight the independant corresponding unit cells Y and cell problems.

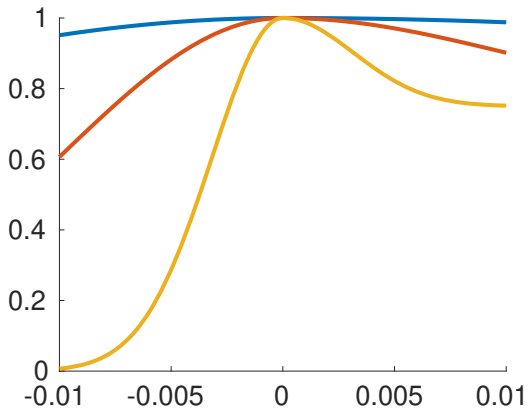

Figure 15: Plots of (12) with parameters $\lambda = 0.75$ and μ = 5e+2 (blue), μ = 5e+3 (red), μ = 5e+4 (yellow), Pe=5000, i.e. v=0.1 [cm s^{-1}].

[10] Institute of Experimental Mineralogy, R.A.o.S.: WWW-MINCRYST: Crystallographic and crystallochemical database for minerals and their structural analogues (2014). URL http://database.iem.ac.ru/mincryst/s_carta.php?CALCITE+706. Accessed: December 18, 2018

[11] Frank, F.: Numerical studies of models for electrokinetic flow and charged solute transport in periodic porous media. Ph.D. thesis, Friedrich-Alexander-Universität Erlangen-Nürnberg (FAU) (2013)

[12] Frank, F.: HyPHM (2014). URL http://www1.am.uni-erlangen.de/HyPHM. Accessed: December 18, 2018

[13] Frank, F., Liu, C., Scanziani, A., Alpak, F.O., Riviere, B.: An energy-based equilibrium contact angle boundary condition on jagged surfaces for phase-field methods. Journal of Colloid and Interface Science **523**, 282 – 291 (2018). DOI https://doi.org/10.1016/j.jcis.2018.02.075. URL http://www.sciencedirect.com/science/article/pii/S0021979718302315

[14] Fries, T.P., Belytschko, T.: The extended/generalized finite element method: An overview of the method and its applications. International Journal for Numerical Methods in Engineering pp. n/a–n/a (2010).

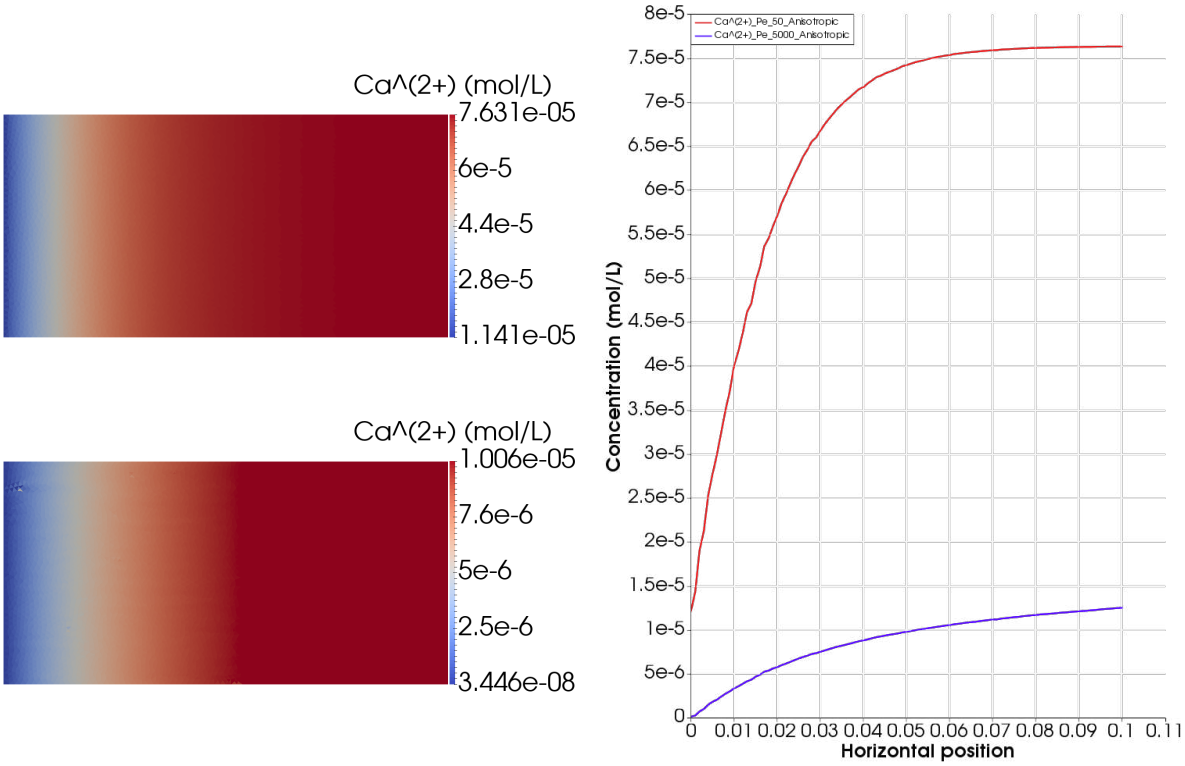

Figure 16: Macroscopic calcium concentrations for different Peclet numbers in the case of anisotropic solid geometry. Top left: Pe = 50, bottom left: Pe = 5000. Right: 1D comparison of values.

DOI 10.1002/nme.2914. URL http://dx.doi.org/10.1002/nme.2914

[15] Frolkovič, P.: Application of level set method for groundwater flow with moving boundary. Adv. Water. Resour. **47**, 56–66 (2012)

[16] Frolkovič, P., Mikula, K.: High-resolution flux-based level set method. SIAM J. Sci. Comp. **29**(2), 579–597 (2007)

[17] Golfier, F., ZARCONE, C., BAZIN, B., Lenormand, R., Lasseux, D., Quintard, M.: On the ability of a darcy-scale model to capture wormhole formation during the dissolution of a porous medium. Journal of Fluid Mechanics **457**, 213–254 (2002). DOI 10.1017/S0022112002007735

[18] Kumar, K., van Noorden, T.L., Pop, I.S.: Effective dispersion equations for reactive flows involving free boundaries at the microscale. Multiscale Modeling & Simulation **9**(1), 29–58 (2011). DOI 10.1137/100804553

[19] Li, X., Huang, H., Meakin, P.: Level set simulation of coupled advection-diffusion and pore structure evolution due to mineral precipitation in porous media. Water Resources Research **44**(12) (2008)

[20] Li, X., Huang, H., Meakin, P.: A three-dimensional level set simulation of coupled reactive transport and precipitation/dissolution. International Journal of Heat and Mass Transfer **53**(13-14), 2908–2923 (2010)

[21] Molins, S.: Reactive interfaces in direct numerical simulation of pore-scale processes. Reviews in Mineralogy and Geochemistry **80**(1), 461–481 (2015)

[22] Molins, S., Trebotich, D., Miller, G.H., Steefel, C.I.: Mineralogical and transport controls on the evolution of porous media texture using direct numerical simulation. Water Resources Research **53**(5), 3645–3661 (2017)

[23] Muntean, A., Van Noorden, T.L.: Corrector estimates for the homogenization of a locally periodic medium with areas of low and high diffusivity. European Journal of Applied Mathematics **24**(5), 657–677 (2013)

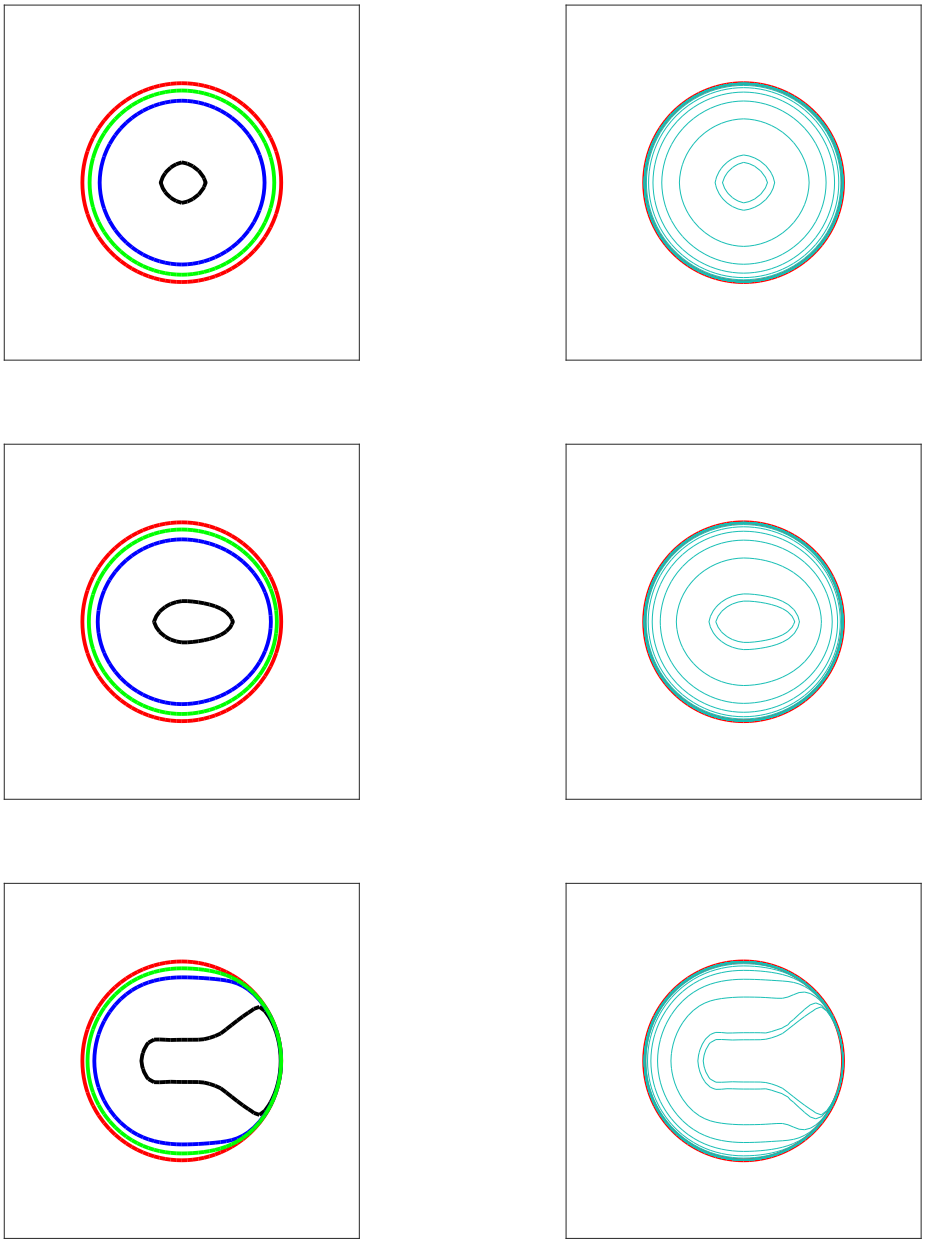

Figure 17: Fluid–solid interface at initial time for all slices (red) and at time T for leftmost slice (black), middle slice (blue), and rightmost slice (green). Simulations done with different parameters for (12). From top to bottom: μ = 5e+2, μ = 5e+3, μ = 5e+4. Evolution is computed with nonequidistant time step sizes.

[24] van Noorden, T.: Crystal precipitation and dissolution in a porous medium: effective equations and numerical experiments. Multiscale Modeling & Simulation **7**(3), 1220–1236 (2009)

[25] van Noorden, T.L., Pop, I., Ebigbo, A., Helmig, R.: An upscaled model for biofilm growth in a thin strip. Water resources research **46**(6) (2010)

[26] Osher, S., Fedkiw, R.: Level set methods and dynamic implicit surfaces, vol. 153. Springer Science & Business Media (2006)

[27] Parvizian, J., Düster, A., Rank, E.: Finite cell method. Computational Mechanics **41**(1), 121–133 (2007). DOI 10.1007/s00466-007-0173-y. URL https://doi.org/10.1007/s00466-007-0173-y

[28] Ray, N., van Noorden, T., Frank, F., Knabner, P.: Multiscale modeling of colloid and fluid dynamics in porous media including an evolving microstructure. Transport in porous media **95**(3), 669–696 (2012)

[29] Ray, N., van Noorden, T., Radu, F., Friess, W., Knabner, P.: Drug release from collagen matrices including an evolving microstructure. ZAMM-Journal of Applied Mathematics and Mechanics/Zeitschrift für Angewandte Mathematik und Mechanik **93**(10-11), 811–822 (2013)

[30] Ray, N., Rupp, A., Prechtel, A.: Discrete-continuum multiscale model for transport, biomass development and solid restructuring in porous media. Advances in Water Resources **107**, 393–404 (2017)

[31] Ray, N., Schulz, R.: Derivation of an effective dispersion model for electroosmotic flow involving free boundaries in a thin strip. Tech. Rep. 398, Preprint Series Angewante Mathematik, Universität Erlangen-Nürnberg (2017). URL http://www.math.fau.de/fileadmin/preprints/pr398.pdf

[32] Redeker, M., Eck, C.: A fast and accurate adaptive solution strategy for two-scale models with continuous inter-scale dependencies. Journal of Computational Physics **240**, 268–283 (2013)

[33] Redeker, M., Rohde, C., Sorin Pop, I.: Upscaling of a tri-phase phase-field model for precipitation in porous media. IMA Journal of Applied Mathematics **81**(5), 898–939 (2016)

[34] Rouy, E., Tourin, A.: A viscosity solutions approach to shape-from-shading. SIAM Journal on Numerical Analysis **29**(3), 867–884 (1992)

[35] Sánchez-Palencia, E.: Non-homogeneous media and vibration theory, *Lecture notes in physics*, vol. 127. Springer-Verlag (1980)

[36] Schmuck, M., Bazant, M.Z.: Homogenization of the poisson–nernst–planck equations for ion transport in charged porous media. SIAM Journal on Applied Mathematics **75**(3), 1369–1401 (2015)

[37] Schmuck, M., Berg, P.: Homogenization of a catalyst layer model for periodically distributed pore geometries in pem fuel cells. Applied Mathematics Research eXpress **2013**(1), 57–78 (2012)

[38] Schulz, R., Knabner, P.: Derivation and analysis of an effective model for biofilm growth in evolving porous media. Mathematical Methods in the Applied Sciences **40**(8), 2930–2948 (2017)

[39] Schulz, R., Knabner, P.: An effective model for biofilm growth made by chemotactical bacteria in evolving porous media. SIAM Journal on Applied Mathematics **77**(5), 1653–1677 (2017)

[40] Schulz, R., Ray, N., Frank, F., Mahato, H., Knabner, P.: Strong solvability up to clogging of an effective diffusion–precipitation model in an evolving porous medium. European Journal of Applied Mathematics **28**(2), 179–207 (2017)

[41] Sethian, J.A.: Level set methods and fast marching methods: evolving interfaces in computational geometry, fluid mechanics, computer vision, and materials science, vol. 3. Cambridge university press (1999)

[42] Soulaine, C., Roman, S., Kovscek, A., Tchelepi, H.A.: Mineral dissolution and wormholing from a pore-scale perspective. Journal of Fluid Mechanics **827**, 457483 (2017). DOI 10.1017/jfm.2017.499

[43] Soulaine, C., Roman, S., Kovscek, A., Tchelepi, H.A.: Pore-scale modelling of multiphase reactive flow: application to mineral dissolution with production of CO_2. Journal of Fluid Mechanics **855**, 616645 (2018). DOI 10.1017/jfm.2018.655

[44] Soulaine, C., Tchelepi, H.A.: Micro-continuum approach for pore-scale simulation

of subsurface processes. Transport in Porous Media **113**(3), 431–456 (2016)

[45] Steefel, C.I., Beckingham, L.E., Landrot, G.: Micro-continuum approaches for modeling pore-scale geochemical processes. Reviews in Mineralogy and Geochemistry **80**(1), 217–246 (2015)

[46] Stumm, W., Morgan, J.J.: Aquatic chemistry: chemical equilibria and rates in natural waters, vol. 126. John Wiley & Sons (1996)

[47] Tartakovsky, A.M., Tartakovsky, D.M., Scheibe, T.D., Meakin, P.: Hybrid simulations of reaction-diffusion systems in porous media. SIAM Journal on Scientific Computing **30**(6), 2799–2816 (2008)

[48] Unverdi, S.O., Tryggvason, G.: A front-tracking method for viscous, incompressible, multi-fluid flows. Journal of Computational Physics **100**(1), 25 – 37 (1992). DOI https://doi.org/10.1016/0021-9991(92)90307-K. URL http://www.sciencedirect.com/science/article/pii/002199919290307K

[49] Van Noorden, T.: Crystal precipitation and dissolution in a thin strip. European Journal of Applied Mathematics **20**(1), 69–91 (2009)

[50] Varloteaux, C., Vu, M.T., Békri, S., Adler, P.M.: Reactive transport in porous media: Pore-network model approach compared to pore-scale model. Phys. Rev. E **87**, 023010 (2013). DOI 10.1103/PhysRevE.87.023010. URL https://link.aps.org/doi/10.1103/PhysRevE.87.023010

[51] Vu, M., Adler, P.: Application of level-set method for deposition in three-dimensional reconstructed porous media. Physical Review E **89**(5), 053301 (2014)

[52] Xiong, Q., Baychev, T.G., Jivkov, A.P.: Review of pore network modelling of porous media: experimental characterisations, network constructions and applications to reactive transport. Journal of contaminant hydrology **192**, 101–117 (2016)

[53] Xu, Z., Huang, H., Li, X., Meakin, P.: Phase field and level set methods for modeling solute precipitation and/or dissolution. Computer Physics Communications **183**(1), 15–19 (2012)

[54] Yoon, H., Kang, Q., Valocchi, A.J.: Lattice boltzmann-based approaches for pore-scale reactive transport. Reviews in Mineralogy and Geochemistry **80**(1), 393–431 (2015)

[55] Zhao, H.K., Chan, T., Merriman, B., Osher, S.: A variational level set approach to multiphase motion. Journal of computational physics **127**(1), 179–195 (1996)

PREPRINTS

DES INSTITUTS FÜR ANGEWANDTE MATHEMATIK (ISSN 1435-5833) BZW. (AB NR. 355) DES DEPARTMENTS MATHEMATIK (ISSN 2194-5127) DER UNIVERSITÄT ERLANGEN-NÜRNBERG

ZULETZT ERSCHIENENE BEITRÄGE:

381 M. Herz, P. Knabner: *Global existence of weak solutions of a model for electrolyte solutions – Part 2: Multicomponent case* (16.05.2014)

382 M. Herz, P. Knabner: *Modeling and simulation of coagulation according to DVLO-theory in a continuum model for electrolyte solutions* (16.05.2014)

383 M. Herz, P. Knabner: *A thermodynamically consistent model for multicomponent electrolyte solutions* (02.06.2014)

384 M. Gahn, P. Knabner, M. Neuss-Radu: *Homogenization of reaction-diffusion processes in a two-component porous medium with a nonlinear flux condition at the interface, and application to metabolic processes in cells* (09.07.2014)

385 J. Jahn: *Directional derivatives in set optimization with the set less order relation* (08.08.2014)

386 N. Ray, P. Knabner: *Upscaling flow and transport in an evolving porous medium with general interaction potentials* (06.10.2014)

387 J. Greifenstein, M. Stingl: *Simultaneous material and topology optimization* (21.10.2014)

388 R. Schulz, N. Ray, F. Frank, H. Mahato, P. Knabner: *Strong solvability up to clogging of an effective diffusion-precipitation model in an evolving porous medium* (06.02.2015)

389 E. Bänsch, A. Brenner: *A-posteriori estimates for the rotational pressure-correction projection method* (29.05.2015)

390 M. Bischoff, J. Jahn: *Economic objectives, uncertainties and decision making in the energy sector* (07.10.2015)

391 R. Schulz, P. Knabner: *Derivation and analysis of an effective model for biofilm growth in evolving porous media* (08.03.2016)

392 M. Gahn, M. Neuss-Radu: *A characterization of relatively compact sets in $L^p(\Omega, B)$* (29.04.2016)

393 N. Ray, A. Rupp, A. Prechtel: *Discrete-continuum continuum multiscale model for transport, biofilm development and solid restructuring in porous media* (26.09.2016)

394 J. Hoffmann, S. Kräutle, P. Knabner: *Existence and uniqueness of a global solution for reactive transport with mineral precipitation-dissolution and aquatic reactions in porous media* (15.11.2016)

395 N. Ray, R. Schulz, A. Rupp, P. Knabner: *Past and present approaches to calculate hydrodynamic parameters in evolving porous media* (16.12.2016)

396 M. Gahn, M. Neuss-Radu, P. Knabner: *Derivation of effective transmission conditions for domains separated by a membrane for different scaling of membrane diffusivity* (22.03.2017)

397 M. Gahn, M. Neuss-Radu, P. Knabner: *Effective transmission conditions for processes through thin heterogeneous layers with nonlinear transmission at the bulk-layer interface* (24.03.2017)

398 N. Ray, R. Schulz: *Derivation of an effective dispersion model for electroosmotic flow involving free boundaries in a thin strip* (31.05.2017)

399 A. Rupp, K.U. Totsche, A. Prechtel, N. Ray: *Discrete-continuum multiphase model for structure formation in soils including electrostatic effects* (28.05.2018)

400 N. Ray, J. Oberlander, P. Frolkovič: *Numerical investigation of a fully coupled micro-macro model for mineral dissolution and precipitation* (18.12.2018)